FOWL PLAY

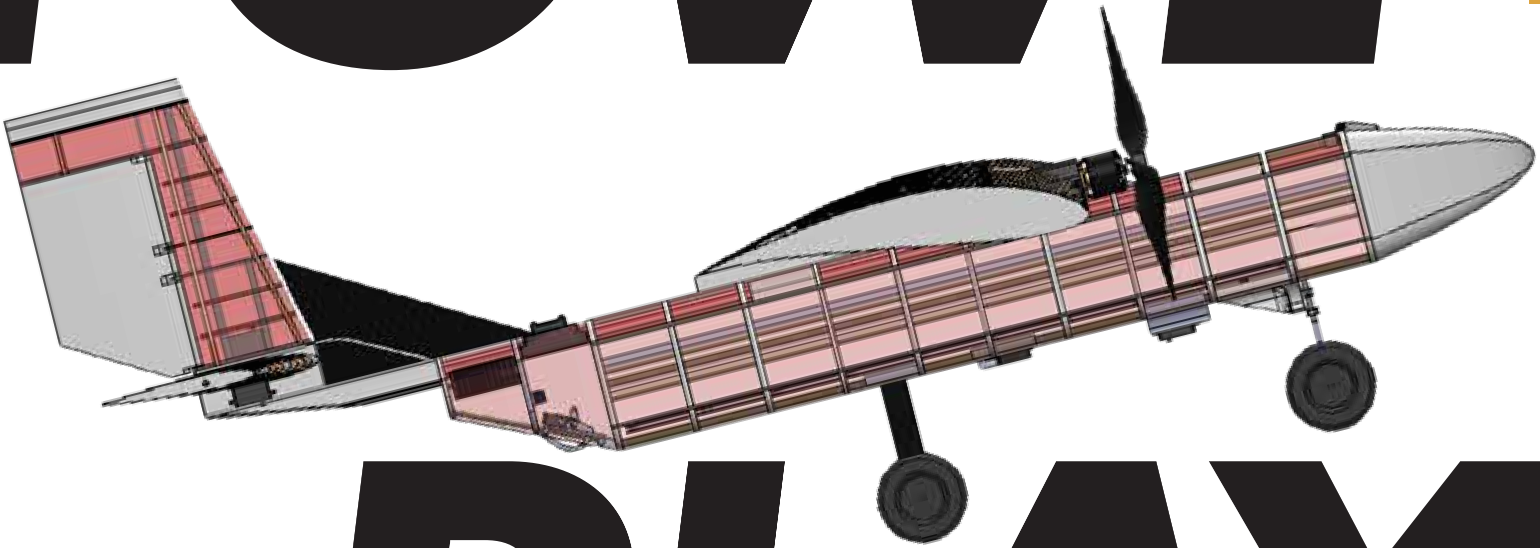

AIAA 2026

DBF DESIGN REPORT

The UNIVERSITY of OKLAHOMA

Table of Contents

Nomenclature

3D	3-Dimensional
A	Amps
ac	Aerodynamic Center
Ah	Amp-hour
AoA	Angle of Attack
AR	Aspect Ratio
ASA	Acrylonitrile Styrene Acrylate
C	Chord of the Wing
c/4	Quarter chord
C_d	Coefficient of drag of a 2D airfoil
C_{li}	Ideal coefficient of lift for a 2D airfoil
$C_{L,cruise}$	Coefficient of lift at cruise speed for a wing
C_{l_β}	Rolling moment due to sideslip angle
$C_{L,max}$	Maximum coefficient of lift for a 3D airfoil
$C_{li,max}$	Ideal coefficient of lift for a 2D airfoil to achieve maximum lift
C_m	Coefficient of moment
C_{m_α}	Rate of pitching moment to angle of attack
C_{m_q}	Rate of pitching moment to pitch rate
C_{n_β}	Rate of yawing moment to sideslip angle
C_{n_r}	Rate of yawing moment to yaw rate
C_{r_df}	Root chord of dorsal fin
C_{root}	Chord length of the root
C_{tip}	Chord length of the tip
cg	Center of gravity
D	Drag
D_{lap}	Lap Distance
Df	Maximum fuselage diameter
$D_{straight}$	Straight Distance
EF	Efficiency Factor
FoM	Figures of merit
ft	feet
g	Acceleration due to gravity
in	Inch
Kc	Correction factor
Kv	Motor Velocity Constant
lbs	Pound(s)
L	Lif
mAh	Milli-Amp Hour
MAC_H	Mean aerodynamic chord of the horizontal tail
MAC_V	Mean aerodynamic chord of the vertical tail
MAC_w	Mean aerodynamic chord of the wing
MAC_X	Used in place of the MAX variables
mph	Miles per hour
mph	Miles per hour
n	Load factor
PETG	Polyethylene Terephthalate Glycol
RPM	Revolutions per Minute
R	Turn radius
S	# of Cells in series in a Battery
$S_{\_df}$	Area of dorsal fin
S1	Max Control Surface Deflection Angle
S2	Max Servo Deflection Angle
t	Time
T_{lap}	Time per lap in seconds
V	Volts
Wh	Watt-hour
WS	Wingspan
ρ	Air Density

1.0 Executive Summary

This report details the design, manufacturing, and testing of *Fowl Play*, the University of Oklahoma's Crimson Skies aircraft for the 2025-2026 American Institute of Aeronautics and Astronautics (AIAA) Design, Build, Fly (DBF) competition. The radio-controlled aircraft was designed to complete four missions to model a bush-style charter and banner deployment operation.

Mission 1 (M1) serves as a proof-of-flight demonstration, verifying that the aircraft can complete a safe and controlled takeoff, flight pattern, and landing. Mission 2 (M2) represents the revenue-generating charter operation. Its purpose is to transport passengers and cargo in separate fuselage bays at the required 3:1 passenger-to-cargo ratio. The score is optimized by increasing the payload amount while completing the highest number of laps feasible. Mission 3 (M3) models a banner-tow operation. Its purpose is to deploy and release a banner in flight. The score is maximized by increasing the released banner length and completing the highest feasible number of laps following successful deployment. Finally, Ground Mission (GM) demonstrates the efficiency of the loading method of the cargo and banner integration system. A mission sensitivity analysis identified payload count in M2 and released banner length in M3 as the dominant score drivers. Accordingly, *Fowl Play* was optimized to maximize payload capacity and banner capability while maintaining reliable low-speed performance and controllability.

Fowl Play is a dual-propeller aircraft with a tricycle landing gear configuration, featuring a conventional tail and a top-mounted rectangular wing. The dual propeller configuration arrangement increases available high static thrust and cruise speed relative to a single tractor configuration. The tricycle landing gear enables banner stowage and release beneath the horizontal stabilizer without ground interference. A high-wing configuration was selected to provide propeller ground clearance, maintain low manufacturing complexity, and maximize payload space within the fuselage. A conventional tail was chosen over alternative configurations to reduce integration risk and ensure predictable longitudinal and directional stability.

The wing consists of lofted airfoil sections with varying incidence angles along the span to manage tip stall progression and improve controllability. The aft fuselage is tapered to reduce unnecessary volume while maximizing usable payload capacity. The cargo bays feature a sliding rack and tray for loading and fastening the Passengers and Cargo within their appropriate bays, internal to the fuselage.

The aircraft was constructed using a combination of materials. The fuselage is composed of additively manufactured ASA frames supported by a carbon fiber hockey stick primary spar, providing bending stiffness and a continuous load path between the wing, landing gear, and empennage. Additional primary structures utilize balsa and carbon fiber spars. The banner was constructed using ripstop nylon to minimize aerodynamic drag while maintaining structural integrity during the tow and release.

Fowl Play had an overall length of 67 in, a wingspan of 60 in, and a maximum height of 28.5 in. The payload configuration was optimized for 48 rubber ducks and 16 hockey pucks. The banner has a target length of 5 ft and a height of 1 ft. Overall aircraft performance is summarized in Table 1.

Table 1: Predicted Performance of Fowl Play

Properties	M1	M2	M3	GM
Take-off Weight (lbs)	15	23.4	15.6	N/A
Mission Time (s)	45	37	54	240
Cruise Speed (mph)	55	65	45	N/A
Number of Laps	3	5	4	N/A
Payload (lbs)	0	8.4	0.6	N/A

2.0 Management Summary

The OU DBF team is a student-managed team from the University of Oklahoma, guided by the faculty advisor and alumni of the team. The team consists of 17 students who participate on an extracurricular basis; 8 are seniors, and 9 of them are underclassmen.

2.1 Team Organization

The OU Crimson Skies team implements a hierarchy similar to those used within the aerospace industry. The management hierarchy for the 2025-2026 team can be found below in Fig. 1.

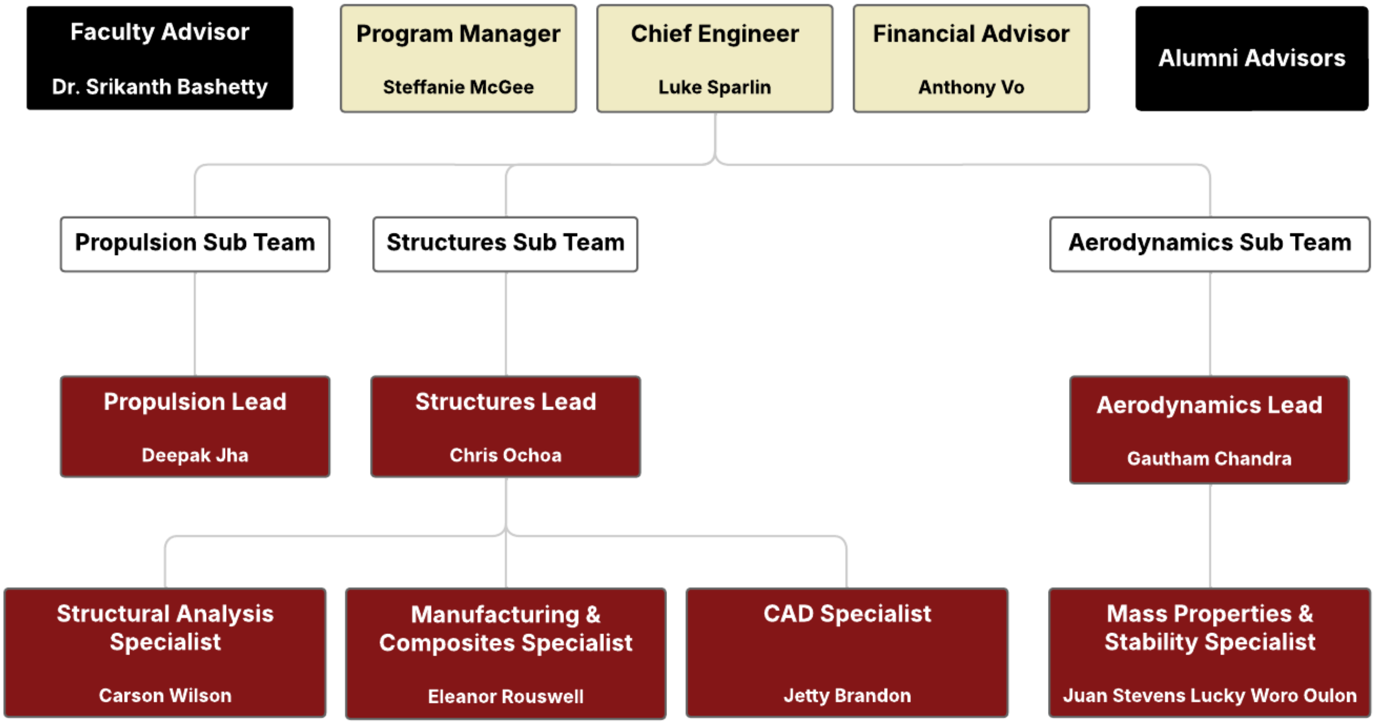

Figure 1: Team Organization Chart

The Chief Engineer directed the team's overall technical execution, including design development, manufacturing, testing, and performance evaluation. The Program Manager: Focused on recruiting and engaging underclassmen, maintaining documentation, facilitating internal communication, and organizing team timelines and milestones. The Financial Advisor: oversaw budget tracking, fundraising activities, purchasing decisions, and coordination of travel logistics for competition.

The three primary officers (Cream) served as the central coordination group, integrating feedback and guidance from faculty and alumni advisors (**Black**) while managing the work of the eight sub-team leaders (**Crimson**). These eight leaders were grouped into three core technical divisions: aerodynamics, structures, and propulsion.

The aerodynamics sub-team handled airfoil selection, overall aircraft sizing, configuration development, and CFD-based aerodynamic performance analysis (Aerodynamics Lead). They also managed aircraft balance, stability analysis, and payload weight determination (Mass Properties & Stability Specialist). Team members in this group required strong fundamentals in aerodynamics, aircraft sizing, stability theory, and experience with CFD and stability analysis software.

The structures sub-team was responsible for designing the fuselage and landing gear, as well as the wing rib and spar architecture (Structures Lead). They supported 3D modeling and additive manufacturing components (CAD & 3D Printing Specialist), conducted FEA and structural validation testing (Structural Analysis Specialist), designed composite molds, and led aircraft fabrication (Manufacturing & Composite Specialist). Members of this team needed expertise in material behavior, aerospace structural analysis, composite fabrication methods, and general manufacturing processes.

Finally, the propulsion sub-team was responsible for propulsion system sizing and integration, propulsion battery selection, and development of the remote banner deployment and release control logic (Propulsion Lead). The Systems Specialist was responsible for the design, integration, and placement of the aircraft's electrical and radio control for the propulsion and banner subsystems. Sub-team members required experience in electrical power system design, propulsion modeling tools, and hands-on electronics skills, such as electrical power system design, propulsion simulation software, and wiring or soldering of electronics.

2.2 Milestone Chart

The Gantt chart shown in Fig. 2 was actively used by the Program Manager to plan, track, and control team progress during weekly team meetings to identify schedule risks, task blockers, and areas requiring resource reallocation. Planned versus actual progress was continuously updated to maintain visibility of design, manufacturing, procurement, and testing deliverables. Key milestones, including prototype manufacturing phases, flight tests, and competition submission deadlines, were tracked with defined completion targets.

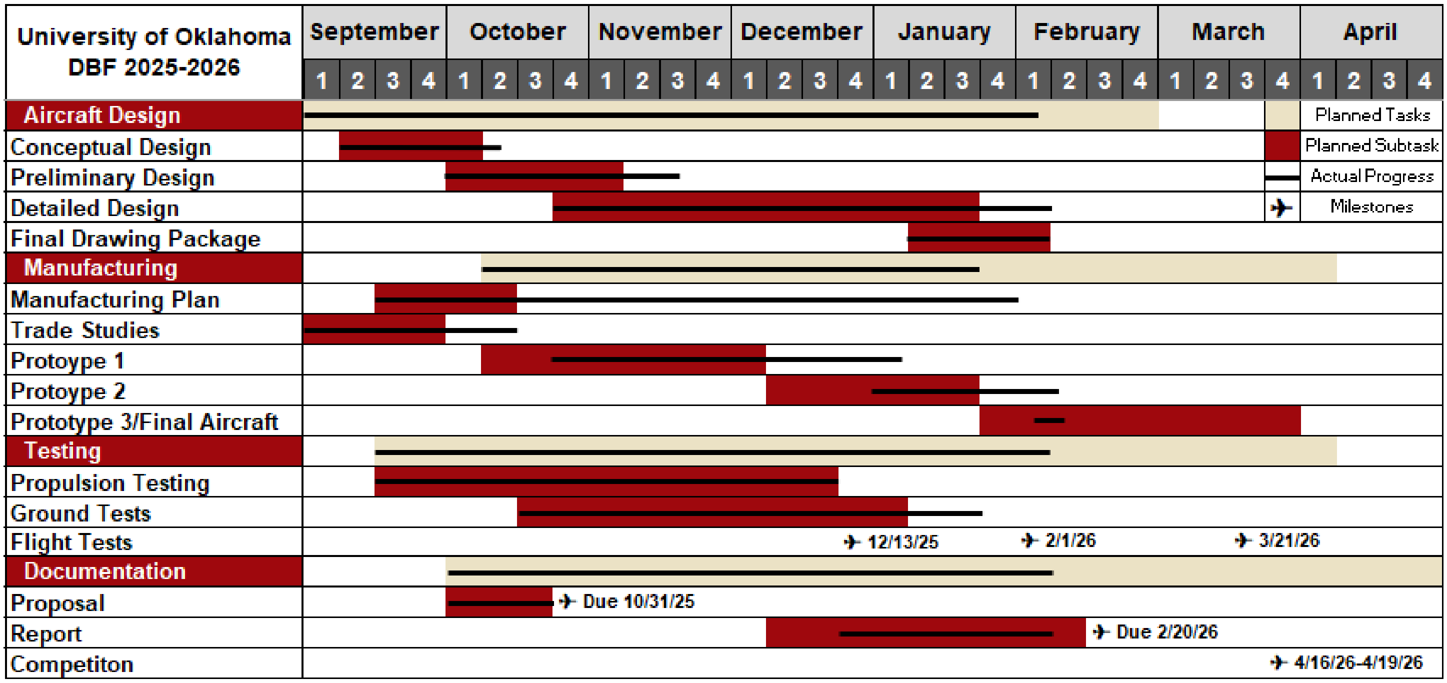

Figure 2: University of Oklahoma's Gantt Chart

3.0 Conceptual Design

3.1 Problem Statement

The AIAA 2025-2026 DBF competition provides the objective for competing teams to design a banner-towing bush plane capable of performing both charter flights and banner towing with the realities of both revenue and costs, ultimately providing a scoring based on net income. The competition offers four missions to be completed. The first is a timed ground mission (GM) demonstrating payload loading/unloading as well as installation, deployment, and release of the banner system. The following three missions include: a test flight to demonstrate airworthiness (M1), a charter flight with payload (passengers and cargo) installed (M2), and a banner flight with deployment and release of the banner (M3).

3.2 Competition Scoring

As written in Eqn. (1), the competition score is the summation of the participation score and the product of the total report score and total mission score, which distinguishes the two primary categories of score sources. Additionally, the participation score offers an opportunity to increase a team's score as follows:

For attending the Fly-off:	Participation score = 1
For completing tech inspection:	Participation score = 2
For attempting a flight mission:	Participation score = 3

$$Competition\ Score = (Total\ Report\ Score\ \cdot Total\ Mission\ Score) + Participation\ Score \tag{1}$$

The total score is weighted such that the proposal accounts for 15% and the design report accounts for 85%. This weighs heavily in favor of a high design report score as shown in Eqn. (2). In the event of a tie between teams, the total report score is further used as the tie breaker, placing emphasis on the importance of a dominant score in this category.

$$Total\ Report\ Score = (0.15\ \cdot Proposal\ Score) + (0.85\ \cdot Design\ Report\ Score) \tag{2}$$

The total mission score is the summation of the three flight missions (M1, M2, and M3) and the GM, which is displayed in Eqn. (3). This category of score is earned at competition rather than as digital submissions.

$$Total\ Mission\ Score = M1 + M2 + M3 + GM \tag{3}$$

3.2.1 Mission 1 – Test Flight

The purpose of M1 is to prove airworthiness via a simple test flight in which a total of three laps must be flown in a pattern as shown in Fig. 3 within a 5-minute window, where the time begins upon advancement of the first take-off attempt. The laps are complete once the aircraft passes over the start/finish line while airborne, such that the third crossing of the line ends the timer, excluding the landing from the timed portion. However, obtaining a score is contingent upon successfully landing the aircraft without bouncing off the runway; rolling off the runway after a controlled landing does not nullify the mission. For M1, the aircraft carries no payload of passengers, cargo, or banner. The scoring is of a binary style in Eqn. (4): 1.0 for pass and 0.0 for fail.

$$M1 = 1.0\ \ for\ successful\ mission \tag{4}$$

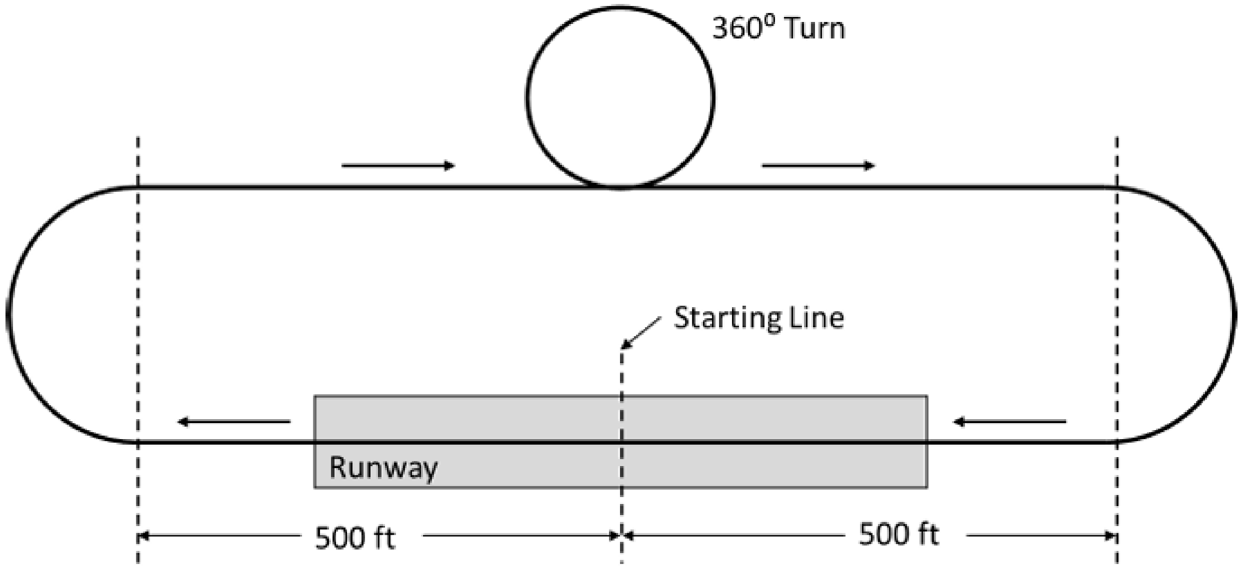

Figure 3: Flight Path for M1, M2, and M3

3.2.2 Mission 2 – Charter Flight

M2 carries a payload of passengers (rubber ducks) and cargo (hockey pucks) that may not exceed the maximum amounts as declared in tech inspection; this mission is also allotted a 5-minute flight window following the same pattern as shown in Fig. 3. As was the case for M1, the time begins as the throttle is advanced for the first take-off attempt, the lap is completed when the aircraft passes the line while airborne, and a score is contingent upon a successful landing. One component of scoring is the efficiency factor (EF), which is a measurement of the capacity of the propulsion battery and represents the associated cost of running a higher propulsion system, calculated using Eqn. (5).

$$EF = \frac{Total\ Propulsion\ Battery\ Capacity\ (Wh)}{100} \tag{5}$$

The EF is considered when calculating the mission cost in Eqn. (6). The cost has an associated multiplier for each lap completed (representing fuel consumption) and units of passenger and cargo (representing added weight), as shown below:

- Base operating cost per lap: C_e = 10
- Passenger operating cost per lap: C_P = 0.5
- Cargo operating cost per lap: C_C = 2

These coefficients are considered in the cost equation., where the product of the passengers and their base cost multiplier, and the product of the cargo and its base cost multiplier, are summed with the base cost of each lap completed. Finally, this sum is multiplied by the number of laps completed and the EF to provide the total cost of operation.

$$Cost = \big(\#laps * \big(Ce + (\#passengers * Cp) + (\#cargo * Cc)\big) * EF\big) \tag{6}$$

In a similar way, the income is calculated with Eqn. (7), which also has an associated multiplier based on the amount of payload (representing more paying customers) and the number of laps that can be made with this payload (representing the distance these passengers can be carried). As shown below, these multipliers far exceed the cost multipliers based on the laps.

- Fixed income per passenger: $l_{p_1} = 6$
- Income per passenger per lap: $l_{p_2} = 2$
- Fixed income per cargo: $l_{c_1} = 10$
- Income per cargo per lap: $l_{c_2} = 8$

Eqn. 7 takes the product of the multiplier per lap for the passengers and the number of laps and adds it to the fixed income per passenger to create a multiplier for the number of passengers. It then does the same for the cargo and sums the two values to calculate the total income of the flight.

$$Income = \left(\#passengers \cdot \left(l_{p_1} + \left(l_{p_2} \cdot \#laps\right)\right)\right) + \left(\#cargo \cdot \left(l_{c_1} + \left(l_{c_2} \cdot \#laps\right)\right)\right) \tag{7}$$

Eqn. (8) subtracts the cost from the income to provide the net income. This results in a final M2 score from Eqn. (9) that is normalized to the maximum competing net income, such that teams may score between 1.0 and 2.0 included.

$$N_{Net_{Income}} = Income - Cost \tag{8}$$

$$M2 = 1 + \left[\frac{N_{Net_{Income}}}{Max_{Net_{Income}}}\right] \tag{9}$$

3.2.3 Mission 3 – Banner Flight

M3 carries a payload of an initially stowed banner that is deployed and released during flight. The deployment occurs after the first upwind turn while traversing the downwind leg of the path; the release occurs upon crossing the finish line on the final lap. As before, the mission occurs in a 5-minute window, which begins upon throttle advancement for the first attempted takeoff, with lap completion occurring after passing the start/finish line while airborne. The landing must be controlled such that the aircraft does not bounce off the runway in order to receive a score for the mission. The rated airplane cost (RAC) is a function of wingspan (WS) such that a larger wingspan results in a higher RAC, as shown in Eqn. (10). The maximum RAC, based on the constraint of a 5 ft wingspan, provides a RAC of 1.0.

$$RAC = (0.05 \cdot WS) + 0.75 \tag{10}$$

The product of the number of laps completed and the length of the banner is divided by the RAC calculated in Eqn. (10). This value is then normalized to the maximum competing team, followed by adding a value of 2.0 such that the highest M3 score cannot exceed 3.0 as shown in Eqn. (11).

$$M3 = 2 + \left[\frac{N\_\frac{\#laps \cdot bannerlength}{RAC}}{Max\_\frac{\#laps \cdot banner\ length}{RAC}}\right] \tag{11}$$

3.2.4 Ground Mission

The GM is a timed event in which the M2 and M3 systems will be demonstrated, with the absence of the propulsion system battery, such that the mechanical payload restraint system (M2) may be demonstrated along with the banner deployment and release system (M3). For M2, a designated crew member will race from a start line to load all passengers and cargo intended for flight and race back to stop the time. Once the pilot demonstrates active flight controls, the crew member will again race to the aircraft, this time to unload the payload and install the stowed banner, returning to the finish line to stop the clock. After demonstrating active flight controls, the crew member will orient the aircraft in a tail-down configuration to allow the pilot to demonstrate banner deployment. As shown in Eqn. (12), the GM score will be the fraction derived from dividing the minimum time ($Min\_(mission\ time)$), the best competing score, by the time achieved by the team ($N\_(mission\ time)$).

$$GM = \left[\frac{Min\_(mission\ time)}{N\_(mission\ time)}\right] \tag{12}$$

3.3 Mission Requirements

The following table extracts requirements from the Mission and Payload Requirements (section 3.1) and the Airplane Requirements (section 3.2) [1]. These are divided into Categories and subcategories based on aircraft components and the system involved; it is further represented in the requirement identification to include

- SAR – System Absolute Requirement – a "must."
- SGR – System Goal Requirement – a "should."
- SG – Subsystem Goal – optimization goal.

Table 2: Mission Requirements & Restraints

Category	Subcategory	Requirement	Req. No.
Main Aircraft	Aerodynamics	Aircraft wingspan must not exceed 5 ft.	SAR-AD-01
		Aircraft must be capable of stable flight in all mission configurations.	SAR-AD-02
		No externally assisted takeoff: all takeoff energy must come from onboard propulsion batteries.	SAR-AD-03
	Structures	Aircraft must pass a wing-tip load test at maximum designed takeoff weight.	SAR-ST-01
		All structure, components, and payloads must be mechanically fastened (no friction-only).	SAR-ST-02
		All aerodynamic surfaces must resist flutter and aeroelastic effects.	SAR-ST-03
		Loaded and empty CG locations must be externally marked.	SAR-ST-04
Mission 2 (Payload)	Passengers	Aircraft must carry at least three standard 2-3-inch rubber duck passengers.	SAR-PL-01
		Passengers must be restrained upright in a single compartment with rigidly attached doors.	SAR-PL-02
	Cargo	Aircraft must carry at least one standard hockey puck in a separated cargo bay.	SAR-CG-01
		Cargo must be restrained and accessed through a single rigidly attached door per bay.	SAR-CG-02

Mission 3	Banner System	Banner must be ≥10 in long with aspect ratio ≤5.	SAR-BN-01
		Banner must externally stow for takeoff without interfering with controls or ground clearance.	SAR-BN-02
		Banner must be remotely deployed, remain vertical in flight, and be remotely released.	SAR-BN-03
Propulsion	General	Aircraft must be propeller-driven and electric powered using unmodified commercial off the shelf motors.	SAR-PP-01
		Propellers must be commercially produced; only tip-clipping, painting, and bore reaming allowed.	SAR-PP-02
	Systems	Each propulsion system must include one battery, one arming fuse, Electronic Speed Controller(s) (ESC), and motor(s).	SAR-PS-01
		Batteries may not be connected in series or parallel; each propulsion system must have its own fuse.	SAR-PS-02
Power	Batteries	Total propulsion energy must be ≤ 100 Wh.	SAR-PW-01
		All battery packs must be unaltered COTS units with visible manufacturer labels.	SAR-PW-02
Safety	Arming	Aircraft must have a mechanical blade-style arming fuse mounted externally on the top surface of the aircraft.	SAR-SF-01
		Arming fuse must be ≥6 in from the propeller plane and accessible without reaching across it.	SAR-SF-02
Avionics	Control Systems	Aircraft must be manually RC-controlled; no autopilots or flight controllers allowed.	SAR-AV-01
		RC system must be commercially available with fail-safe and operate on legal US frequencies.	SAR-AV-02
Operations	General	Aircraft takeoff gross weight ust be <55 lb.	SAR-OP-01
	Banner Operations	A second transmitter may be used for banner deployment only operated by the observer.	SAR-OP-02

3.3.2 Sensitivity Analysis

A sensitivity study was performed for both M2 and M3 to determine the most heavily weighted items for which to optimize to increase scoring effectively. The sensitivity analysis for M2 identified the importance of high fuselage volume to increase payload capacity against the importance of speed for increased lap count; because both payload numbers and lap count increase income as shown in Eqn. (7), it is necessary to understand the parameter for which to optimize. The sensitivity analysis for M3 contrasts the impact of the banner length against the number of laps, which directly affects aircraft speed. As before, it is important to identify the more impactful factor, as both result in an increase in score.

For M2, Fig. 4 displays the sensitivity analysis derived using Excel. After selecting some payload count and lap count, a chart can be used to display how an increase or decrease in the percentage of either counts will affect the mission score. As shown in the figure, a 20% increase in payload provides around a 20% increase in the mission score; however, the same increase in lap count only provides about a 13% increase in the mission score. This occurs for our predetermined payload count of 51 ducks and 17 pucks with an estimated lap count of 5 laps; this benefit in increased payload holds true for all practical values tested. The obvious increase in score for increase payload count leads to the optimization of a high payload capacity, resulting in the need for a high, internal volume aircraft and influencing our design as such.

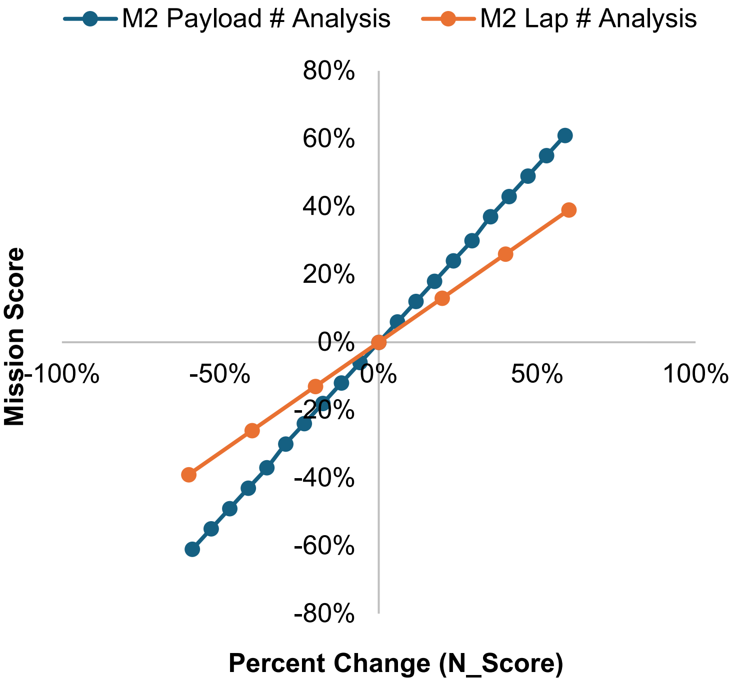

Figure 4: Mission 2 sensitivity analysis

Similarly, Fig. 5 displays the sensitivity analysis for M3. After selecting some banner length and lap count, a chart can be used to display how an increase or decrease in the percentage of either the length or count will affect the mission score. As shown in the figure, a 20% increase in banner length provides around a 20% increase in the mission score; the same is true for the lap count increase and result. This occurs for our predetermined banner length of 60 inches with an estimated lap count of 5 laps. The alignment of the two slopes holds true for all practical values tested. This alignment also derives the result that optimizing for either banner length or lap count will result in a similar score increase. Because M2 optimized for internal volume over speed, M3 is affected by this design choice such that speed was forgone and banner length was selected for which to be optimized.

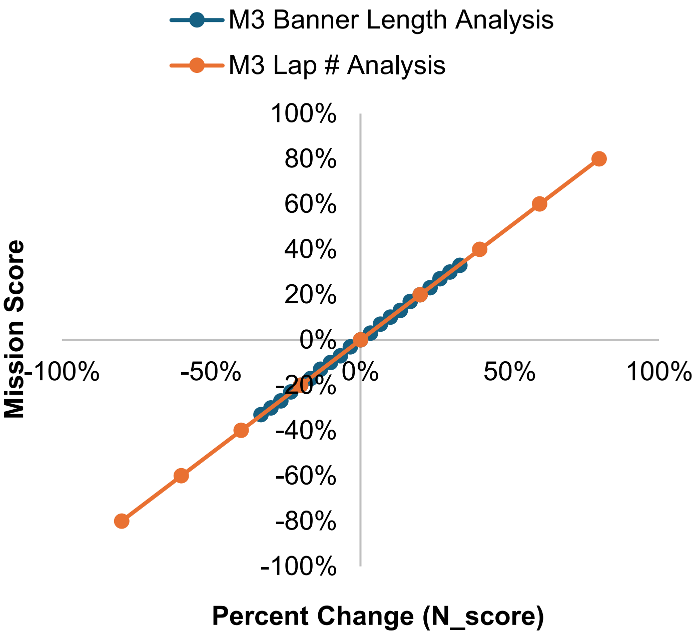

Figure 5: Mission 3 sensitivity analysis

3.4 Aircraft Configuration Trade Studies

3.4.1 Wing Placement

The three wing placement options considered in the design phase are identified in Table 3. The manufacturability of the wing configuration was highly weighted to ensure a short manufacturing lead time. Cargo accessibility was strongly considered as ease of access directly contributes to increasing GM score. The structural design was considered to minimize component failure. Stability and control were examined to offer consistent aerodynamic performance and ease pilot workload with the desired 8.4 lb payload. The mid-wing placement was eliminated due to the difficulty in manufacturing. While low wing placement offered high structural integrity and manufacturability, the concerns of rolling stability with a heavy payload eliminated this option. The high wing placement was selected because of its ease of manufacturing and stability characteristics for high-lift cargo-style aircraft in both loaded and unloaded scenarios.

Table 3: Wing Placement Decision Matrix

		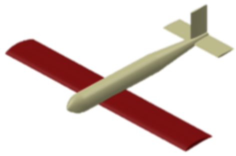	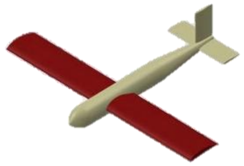	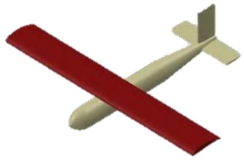
Figures of Merit	**Factor**	**Low Wing**	**Mid Wing**	**High Wing**
Structural Design	0.2	8	6	8
Manufacturability	0.3	6	4	7
Fuselage accessibility	0.3	7	7	10
Stability & Control	0.2	8	6	8
Total		7.1	5.7	8.3

3.4.2 Fuselage configuration

Table 4 shows the two fuselage configurations considered: conventional and boom. Manufacturability and weight reduction were highly weighted to ensure an efficient and practical design. The boom design was eliminated because of its limited internal cargo volume. The conventional tail was selected for its optimal storage capability for the passengers and cargo.

Table 4: Fuselage Confirmation Matrix

			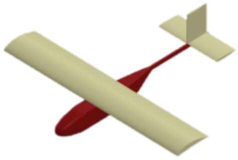
Figures of Merit	**Factor**	**Conventional**	**Boom Tail**
Payload Bay	0.3	8	5
Manufacturability	0.2	7	6
Stability & Control	0.3	7	7
Weight	0.2	4	7
Total		6.3	5.5

3.4.3 Tail Configuration

The four tail configurations examined are highlighted in Table 5. Ease of manufacturing and stability were key factors in the selection process to ensure a well-balanced design. The V-tail was quickly discarded due to its complex manufacturing requirements, despite its favorable weight characteristics. The H-tail offered potential stability, particularly in yaw attitude, and drag reduction. However, its increased weight and decreased manufacturability led to its dismissal. The T-tail provided improved horizontal stability and greater efficiency by positioning the horizontal stabilizer outside the wing's wake, but the required reinforcement of the vertical stabilizer negated its weight advantages. A conventional tail design was selected for its ease of manufacturing, adequate stability, and overall lightweight design.

Table 5: Tail Configuration Decision Matrix

		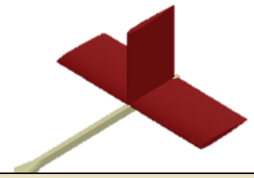			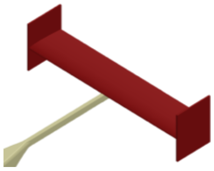
Figures of Merit	**Factor**	**Conventional**	**T-Tail**	**V-Tail**	**H-Tail**
Structural Design	0.2	7	7	4	6
Manufacturability	0.3	7	6	2	5
Weight	0.3	5	5	9	2
Stability & Control	0.2	5	7	4	9
Total		7.1	6	6.3	4.4

3.4.4 Propulsion Configuration

Three primary propulsion configurations were evaluated for the DBF aircraft: a single nose-mounted tractor, a single pusher, and a twin wing-mounted tractor arrangement. These configurations were compared and analyzed based on factors such as maximum thrust, interference with payload mechanisms, ease of construction, stability, etc. A single nose-mounted tractor configuration offers mechanical simplicity, low system mass, and efficient propeller operation in clean, undisturbed inflow; however, it limits access to the fuselage for cargo and passenger loading. Additionally, a nose-mounted tractor also loses propulsive efficiency due to flow blockages by the fuselage. A single pusher configuration improves forward fuselage packaging and reduces propeller-induced airflow over the wing and control surfaces but had to be ruled out to account for banner towing, it also suffers from reduced propulsive efficiency due to inflow interference from the fuselage and wing, as well as increased cooling and structural integration challenges. On the other hand, the twin wing-mounted tractor configuration provided higher total static thrust, improved redundancy, and enhanced low-speed control authority due to propeller slipstream over the wing. Additionally, this configuration improved lateral stability when the twin-propellers are counterrotating. While the twin-motor configuration introduces additional complexity and weight relative to a single-motor, its superior thrust capability, controllability, and allowance for better fuselage access made it the most suitable choice. A detailed trade study is shown in Table 6 below.

Table 6: Propulsion Configuration Decision Matrix

		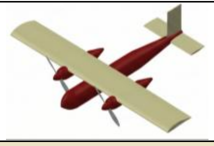	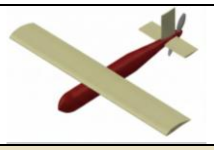	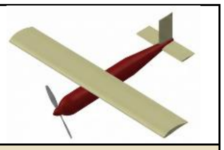
Figures of Merit	**Factor**	**Twin-prop**	**Pusher**	**Nose Tractor**
Max. Thrust	0.20	9	6	4
Payload Interference	0.15	8	9	6
Stability	0.20	9	4	6
Construction	0.10	6	6	8

Propwash Benefits	0.20	9	2	2
Safety	0.15	9	2	2
Total Score		**8.55**	4.65	4.40

3.4.5 Landing Gear Configuration

Table 7 shows the landing gear configurations considered, including tricycle and taildragger. Stability, structural strength, and banner compatibility were key factors in the selection process. A taildragger configuration was not selected due to potential difficulties in handling due to increased risk of nose-over incidents during landing, as well as concerns of an aerodynamic center-mounted banner tangling with the tailwheel. The tricycle landing gear configuration was chosen for its improved handling during landing and overall stability, alongside the wide stance which leaves ample room for the banner. This design ensures reliable ground operations while minimizing stress on the aircraft structure.

Table 7: Landing Gear Decision Matrix

		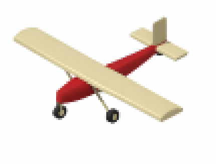	
Figures of Merit	**Factor**	**Tricycle**	**Tail Dragger**
Structural Design	0.3	4	3
Manufacturability	0.3	3	4
Weight	0.1	3	2
Drag	0.2	3	3
Banner Compatibility	0.4	5	2
Total		**5.0**	3.7

3.4.6 Payload and Cargo Configuration

Table 8 shows the passenger fastening configurations considered: head constraint and floor & head constraint combined. Constraint Stiffness was the highest weight to ensure passenger security. The floor & head constraint was selected due to its stiffness and minimal weight difference compared to the head constraint.

Table 8: Payload Configuration Decision Matrix

		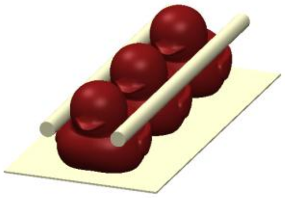	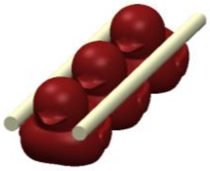
Figures of Merit	**Factor**	**Floor & Head Constraint**	**Head Constraint**
Manufacturability	0.3	8	8
Weight	0.2	5	8
Constraint Stiffness	0.5	8	5
Total		7.4	6.5

Table 9 shows the cargo storage configurations considered: a box tray and a two-sheet tray. Constraint Stiffness was the highest weight to ensure cargo security. The two-sheet tray was selected due to its weight and manufacturability advantages.

Table 9: Cargo Configuration Decision Matrix

		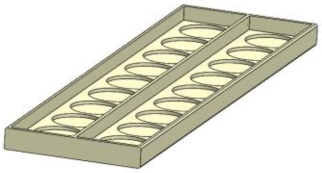	
Figures of Merit	**Factor**	**Box Tray**	**Two Sheet Tray**
Manufacturability	0.3	7	8
Weight	0.2	6	8
Constraint Stiffness	0.5	9	8
Total		7.8	8

3.4.7 Banner Material Configuration

The selection of the banner material for Mission 3 was driven by the need to minimize aerodynamic drag while maintaining sufficient structural integrity during towing, deployment, and release. Because the banner contributes directly to aircraft drag and therefore mission performance, material properties such as stiffness, surface smoothness, mass, and cost were evaluated through a trade study. Several candidate materials were considered, including vinyl, polypropylene, polyester, and ripstop nylon. Vinyl offers high durability and stiffness, but was found to be prohibitively heavy, resulting in increased drag and a significant penalty to aircraft performance. Polypropylene (PP) and polyester fabrics provided moderate weight savings; however, their relatively low elastic modulus led to excessive flutter during preliminary testing, increasing unsteady aerodynamic loads and drag. Ripstop nylon was ultimately selected as the banner material due to its favorable balance of stiffness, low areal density, and cost. With a relatively high Young's modulus compared to other lightweight fabrics, ripstop nylon reduces banner flutter during towing, thereby decreasing induced and unsteady drag. Additionally, its low mass (approximately 1.2 oz/yd²) minimizes the weight penalty imposed on the aircraft, improving mission endurance and handling characteristics. This trade study can be viewed in Table 10.

Table 10: Banner Material Trade Study

Factors of Merit	wt.	Vinyl	PP	Polyester	Ripstop
Cost ($/roll)	0.2	~12.0	**~7.0**	~10.0	~8.0
Weight (oz/sq.yd)	0.4	9.0	2.5	3.0	**1.2**
Young's Modulus (MPa)	0.4	300	1500	2000	**3000**
Viability Score	—	21.0	59.2	56.7	**97.5**

3.4.8 Banner Deployment Mechanism Configuration

Table 11: Banner Stow Mechanism Trade Study

Factors of Merit	wt.	Rod Flat	Rod Up	Canister	Tucked
Manufacturing	0.3	3	1	2	**4**
Interference	0.1	3	2	1	**4**
Complexity	0.3	4	3	**1**	2
Detachment	0.3	3	3	2	**1**
Viability Score	—	**82.5**	57.5	40.0	62.5

Several different stowing and deployment mechanisms were compared based on their ease of manufacturing, complexity, interference with the fuselage, and ease of detachment. Based on the comparison shown in Table 11, the Flat-Rod mechanism was deemed optimal. The design entails the banner being attached to a rotating rod mounted between bearings, which allows it to unfurl naturally under aerodynamic drag. The flat, wing-parallel orientation of the rod minimizes interference with the fuselage, reduces drag penalties, and simplifies integration with the tricycle landing gear.

4.0 Preliminary Design

4.1 Design Methodology

The aircraft was developed using an iterative, requirements-driven methodology informed by past DBF designs and systems-engineering practices. Mission rules and scoring sensitivities were analyzed in Excel, identifying payload capacity, and thus banner length, as the primary driver. This led to selecting a high-wing, conventional-tail, twin-prop configuration for stability, internal volume, and controllability. Preliminary design combined Excel-based mission predictions with aerodynamic analysis in XFLR5. Propulsion sizing used eCalc, thrust-stand measurements, and installed static testing to validate performance. Structural loading for the fuselage and landing gear was evaluated in ANSYS with appropriate safety factors. Detailed design was completed in SolidWorks, integrating internal structures, payload bays, and the banner system. Iteration during this phase produced a redesigned wing with geometric twist to shift stall inboard and improve controllability, along with lowered landing gear to reduce top-heaviness. Manufacturing began with composite wings, 3D-printed components, balsa structures, and carbon-fiber spars, later transitioning to modular non-composite construction to support rapid prototyping. Ground testing, including taxi trials and propulsion validation, provided data used to refine aerodynamic and structural predictions. This iterative process ensured the final aircraft met all mission and performance requirements and can be seen in Fig. 6.

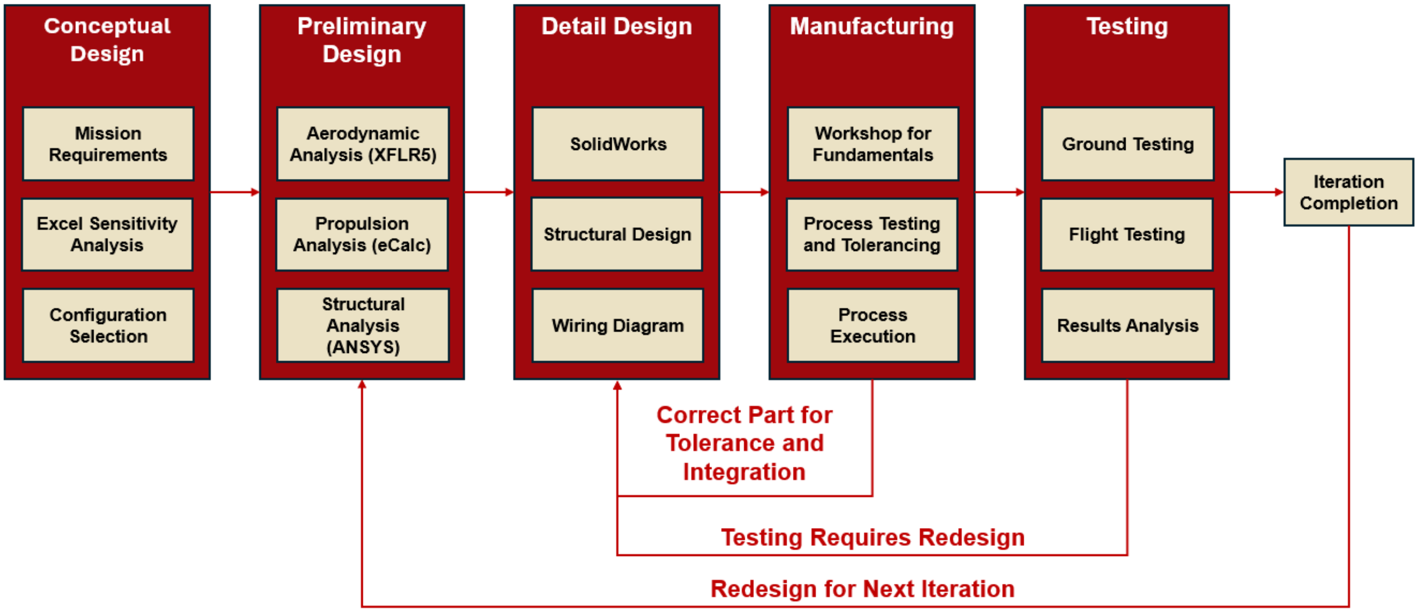

Figure 6: Design Methodology

4.2 Flight Path

Fig. 7 provides a visual representation of the required flight path, beginning at takeoff and traveling 500 ft at 150 ft before turning crosswind and then downwind. Once reaching midfield, the aircraft will make a 360° loop before continuing another 500 ft downwind. After turning base and final, the aircraft will travel upwind before crossing the start/finish line, completing one lap. The preceding sections will discuss the design to ensure the aircraft can complete the flight path in the relevant configurations successfully.

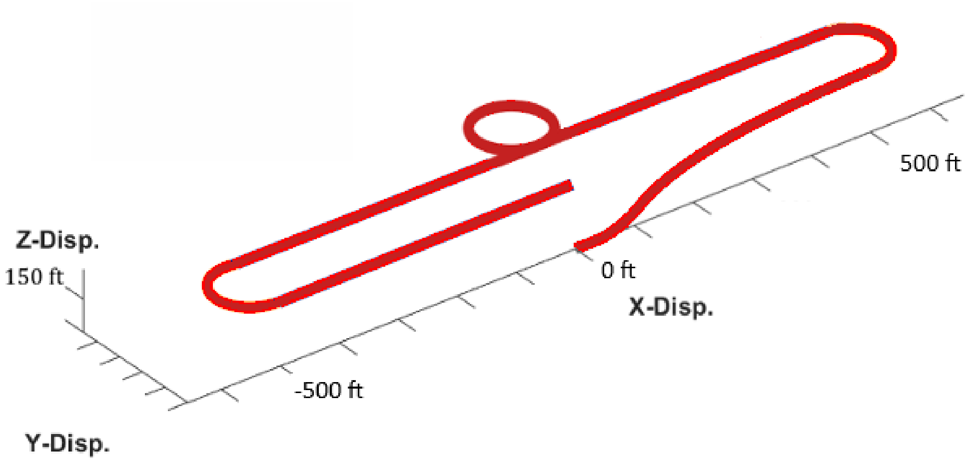

Figure 7: Flight Path

4.3 Aerodynamics

4.3.1 Wing sizing and geometry

The team set parameters the aircraft would need to meet for the required lift (L), stall velocity (V_s), and cruise velocity (V). The aircraft's maximum weight was set at 45 lbs. Trade studies of similar DBF competitions yielded a V of 70 mph with a max velocity of 80-85 mph. A V of 65 mph was determined to balance payload carrying capacity with safe landing capabilities. To generate the lift needed to meet the steep weight requirements, the maximum allowed wingspan of 5 ft was used. Using a wing loading chart shown as shown in Table 12 by, Lennon [2], a chord of 18 in was used to closely relate to the recommended wing loading value for a moderate speed aircraft.

Table 12: Recommended Wing Loading Values by Lennon [2]

Model Type	Wing Loading oz./sq-ft
High speed, high maneuverability	22 - 26
Moderate speed sport	16 - 22
Low speed trainer	12 - 16

Using an aspect ratio (AR) of 3.33 was chosen, as a medium AR would give the aircraft a good balance of lift production, maneuverability, and drag reduction. With an AR of 3.33, this would make the Mean Aerodynamic Chord (MAC) of the wing 1. 5 ft, and the planform area of the wing (S) 7.5 ft^2.

The chosen parameters and outlined geometry in previous section provided information to calculate the required C_L of the wing which allowed for an airfoil selection. The $C_{L,cruise}$ at cruise speed and $C_{L,max}$ at stall speed were found with the following equations.

$$C_{L,cruise} = \frac{L}{0.5 \cdot \rho \cdot V_{cruise}^2 \cdot S} \tag{13}$$

$$C_{L,max} = \frac{L}{0.5 \cdot \rho \cdot V_{stall}^2 \cdot S} \tag{14}$$

The aircraft was assumed to be flying at sea level in steady, level, unaccelerated flight (SLUF). From this assumption the lift required is equal to the weight of the aircraft, yielding a required lift of 45 lb. From Eqn. (14), $C_{L,max}$ = 2.2. Since these calculations were done for a 3D wing, a correction factor needed to be applied to transfer the 3D coefficients to a 2D airfoil resulting in the ideal coefficient of lift (C_{li}). This gives us the minimum C_l required for the airfoil to result in the $C_{L,cruise}$, initially calculated. C_L is divided by a factor of 0.855, taken from Sadraey [3]

$$C_{li} = \frac{C_L}{0.855} \tag{15}$$

This This equation. was used to determine the required lift coefficients of $C_{l,\text{cruise}} = 0.8$and $C_{l,\max} = 1.3$. To ensure sufficient lift generation, only airfoils exceeding these minimum C_l requirements were considered. This conservative approach accounted for uncertainty in wing geometry evolution and provided margin for potential increases in payload mass to improve the Mission 2 score.

An initial screening of approximately 100 airfoils was conducted using XFLR5. From this analysis, four candidate airfoils were selected based on high $C_l$capability and favorable lift-to-drag (L/D) ratios at cruise conditions: the Eppler 398, Eppler 561, Göttingen 502, and Göttingen 176.

The aerodynamic characteristics of these airfoils are shown in Figs. 8 and 9. Figure 8 presents the $C_l$versus angle of attack curves, where the Eppler 398 demonstrates the highest $C_{l,\max}$ among the candidates. Figure 9 illustrates the corresponding lift distributions, with the Eppler 398 exhibiting the most favorable overall lift characteristics. Based on this analysis, the Eppler 398 was selected as the primary wing airfoil.

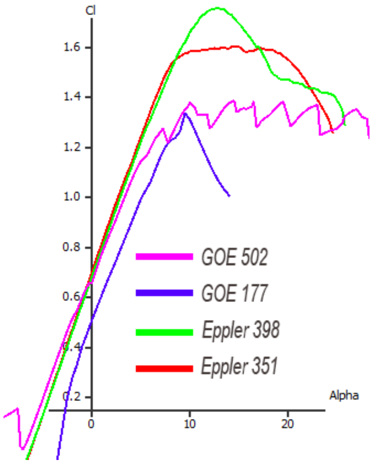

Figure 8: Cl vs Alpha of selected airfoils

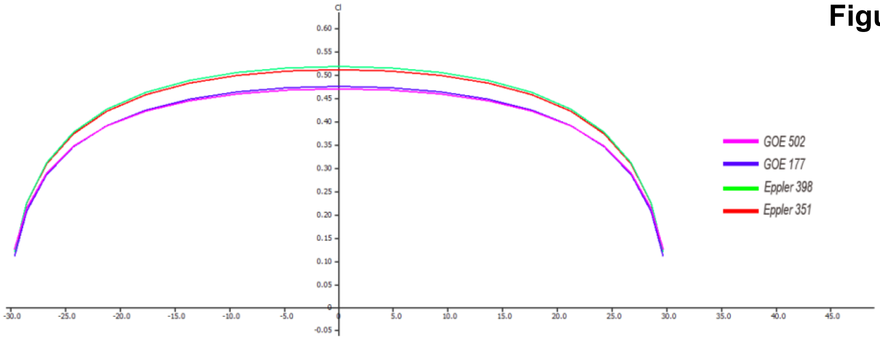

Figure 9: Spanwise Cl distribution across wing for different airfoils

4.3.2 Tail sizing and geometry

Tail sizing was conducted following the steps, equations, and recommendations provided by Sadraey [3]. Volume coefficients were used to find the optimal tail arm length (l) and planform area (S) for both the vertical and horizontal stabilizers, defined by the variables V_V and V_H respectively. Table 13 was used to determine these coefficients. The values chosen were 0.8 for V_H and 0.07 for V_V, matching the dual prop configuration. Eqn. (16) was used to determine the horizontal tail area with the wing area and the tail moment arm. This gave an ideal horizontal tail area of 223 in^2.

$$HTA = \frac{2.5*MAC*20\%*WA}{TMA} \tag{16}$$

From this, the chord and span were acquired using Eqns. (17) and (1)8. To have the tail appropriately sized, the aspect ratio was kept between 3 and 5. This yields a chord of 7 in and a span of 33 in.

$$b = \sqrt{A*S} \tag{17}$$

$$c = \frac{S}{WS} \tag{18}$$

The volume coefficient method was used to size the vertical stabilizer, represented by Eqn. (19). To match the V_v value selected from Table 3, the area of the vertical stabilizer was chosen to be 1/8 the area of the main wing, which yielded a value of 120 in^2. Using Eqn.s 17 and 18, the height and chord of the vertical tail were found to be 18 in and 8.5 in, respectively. To ensure that the tail of the aircraft is efficient, a taper ratio of 0.7 was selected as recommended by Lennon [2]. To enhance directional stability and prevent rudder blanketing at high angles of sideslip, a dorsal strake was integrated into the tail design. Following the geometric proportions seen in heavy-lift aircraft, the strake serves to increase the effective vertical surface area without significantly increasing the aircraft's height. This addition ensures the vertical tail remains effective even when the fuselage creates a turbulent wake at high angles of attack.

$$V_v = \frac{S_v * L_v}{S_w * b_w} \tag{19}$$

Table 13: Common Horizontal & Vertical Tail

Aircraft	V_H	V_V
Glider/ Motor Glider	0.6	0.03
Home-built	0.5	0.04
GA Single Prop Engine	0.7	0.04
GA Twin Prop Engine	0.8	0.07
GA with Canard	0.6	0.05
Agricultural	0.5	0.04
Twin Turboprop	0.9	0.08
Jet Trainer	0.7	0.06

In order to account for crosswind conditions in Wichita, Kansas, it was judged optimal to design a dorsal fin to allow the vertical tail to operate safely at larger sideslip angles. The dorsal fin increases directional stability at high sideslip by delaying vertical tail stall and improving flow attachment at the vertical tail root. The fin design methodology was based on the statistical empennage sizing methods presented by Scholz [5]. Among the available methods, Method 2 for jet-powered aircraft was selected. This method was chosen because it demonstrated one of the highest reported coefficients of determination (R^2) in the statistical regression analysis and yielded geometrically reasonable values for a small-scale DBF configuration.

Method 2 determines the dorsal fin geometry using statistically derived correlations based on vertical tail area and root chord. For jet aircraft, the following relationships are used [5]:

$$S_{df} = 0.106\, S_v \tag{20}$$

$$C_{r_{df}} = 0.575\ \ C_{r_v} \tag{21}$$

In order to incorporate the part to the aircraft design, the dimensions obtained from the sizing method were extrapolated to flush in with the fuselage.

4.3.3 Control Surface Sizing

The primary control surfaces on the aircraft were chosen to be ailerons, an elevator, and a rudder. Flaps were considered easier takeoff and landing by the pilot, however adding flaps would lead to an increase in weight and complexity of the design, thus they were eliminated from consideration. Flaperons were also considered, but due to the added risk of fluttering from such a large control surface size it was eliminated. Ailerons provided adequate roll authority without the added manufacturing complexity and flutter risk of other considered design. The control surface sizes followed the recommendations outlined by Sadraey [3]. The aileron chord size was selected to be 25% of the chord of the wing, maximizing the recommended size of 15-25%. The ailerons were located at 50% to 90% of the wingspan for each side of the wing. This resulted in an aileron span of 40% which is much larger than the recommended textbook value of between 20-30%. The elevator and rudder chords were recommended to be between 20-50% of the chord of their respective stabilizer, and their span to be 90% of the stabilizer span. A chord of 35% of their stabilizer chords for both the rudder and elevator as a good middle ground, which allowed future changes to the size as needed after testing.

4.3.4 Wing Twist Study

To ensure the aircraft maintains controllability during high angle-of-attack maneuvers and landing phases, a -5° geometric twist washout was integrated into the wing design. This design choice serves as the primary method for managing spanwise lift distribution and preventing the hazardous tip-stall behavior observed in earlier iterations. By decreasing the angle of incidence toward the wingtips, the design forces the root chord to reach its critical angle of attack and stall before the tips, thereby preserving aileron effectiveness even as the wing begins to lose lift.

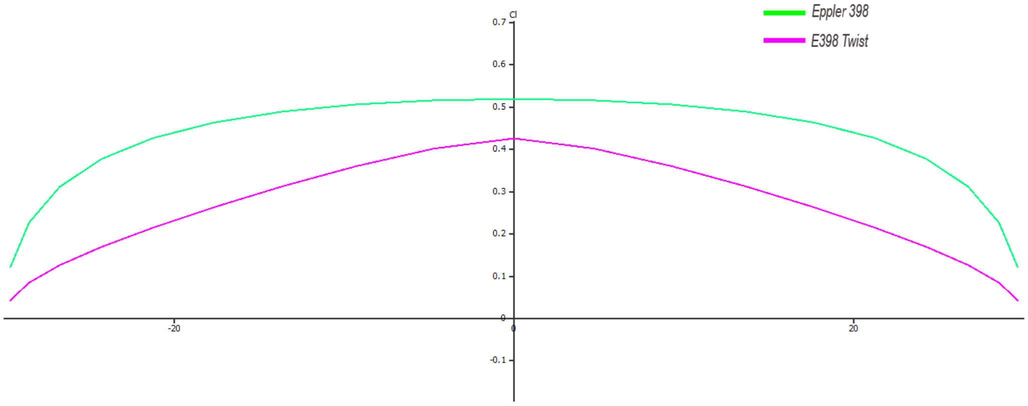

Figure 10: Spanwise Cl distribution for wing twist study

Fig. 10 showcases the results of the Lifting Line Theory comparing four different wing twist configurations. As recommended by Sadraey [3], a -5° twist was incorporated into the Eppler 398 wing profile, which successfully reduced the tip lift but failed to provide the aggressive safety margin required for the mission profile. At 0° angle of attack, the wingtips produce negative lift. This indicates that the tips are operating at a significantly lower effective angle of attack than the root, providing a buffer that ensures that the ailerons remain functional during deep-stall maneuvers or slow-speed landing approaches.

4.3.5 Wing fences and endplates trade study using CFD

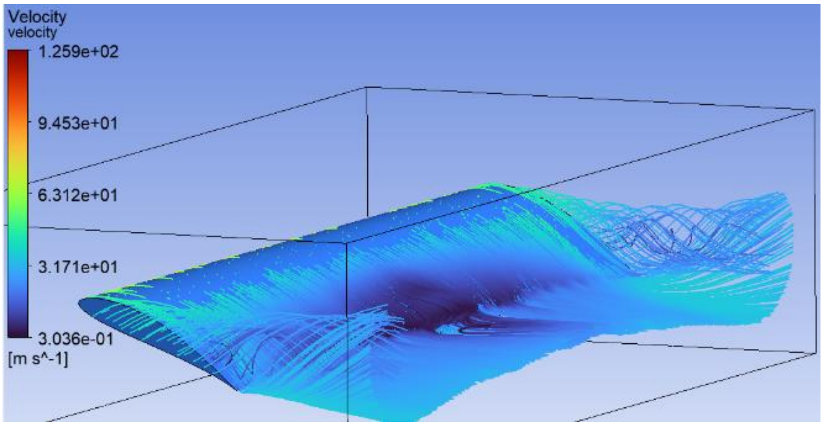

Figure 11: Base Wing Flow Separation at Takeoff Conditions and High AoA

During early analysis and testing of the baseline wing configuration, the aircraft behavior showed undesirable tip stall, resulting in reduced roll authority near slow flight. This occurred despite the use of a constant chord and airfoil along the span, indicating that three-dimensional effects were dominating the stall behavior. Observations suggested that vortices toward the wingtip at high angles of attack was contributing to early flow separation in the outboard wing sections, a phenomenon commonly observed on finite wings operating near stall. CFD on ANSYS was used to confirm this observation at takeoff condition with high AoA (25°) in Fig. 11 [3].

Because increasing geometric twist or redesigning the wing planform would have introduced additional structural and manufacturing complexity, the team looked into passive flow control devices as a way to resolve the issue. Wing fences were identified as a promising solution due to their ability to locally inhibit spanwise flow and improve stall progression without requiring major wing redesign. Flight and wind-tunnel investigations have shown that wing fences can delay outboard separation and improve lateral control near stall by forcing the flow to remain more chordwise, particularly on wings operating at high lift coefficients [7]

Based on these findings, a CFD analysis was performed with wing fences were positioned outboard of mid-span and inboard of the ailerons to address the observed stall behavior while maintaining control surface effectiveness. This placement method relied on documented fence implementations where the goal is to protect outboard sections from early stalls. [7,8]

In parallel, wingtip endplates were investigated to improve induced-drag performance and reduce wingtip vortex strength during slow flight. Studies on finite-wing aerodynamics have demonstrated that endplates increase the effective aspect ratio and reduce induced drag at high lift coefficients, making them particularly effective for low-speed, high-lift operation [9,10]. Endplates were therefore designed to be thin and lightweight to minimize parasitic drag and structural penalties while improving aerodynamic efficiency.

Three-dimensional CFD simulations were conducted using ANSYS to evaluate the baseline wing, wing fence configuration, endplate configuration, and the combined design. Simulations were performed at slow-flight and near-stall conditions, consistent with recommended practices for low-Re wing analysis [3]. Mesh refinement was done near the leading edge, wingtip, and flow-control devices to accurately capture separation and vortex behavior. Output quantities included lift and drag coefficients, and surface flow visualization.

Simulation results did not give enough substantiation to justify the use of wing fences for improved stall. Instead, they created a notable increase in drag and decrease in lift and a visible higher flow separation occurring like Figure 12 shows. Compared to the original design, CL was 11% lower and CD was 57% higher.

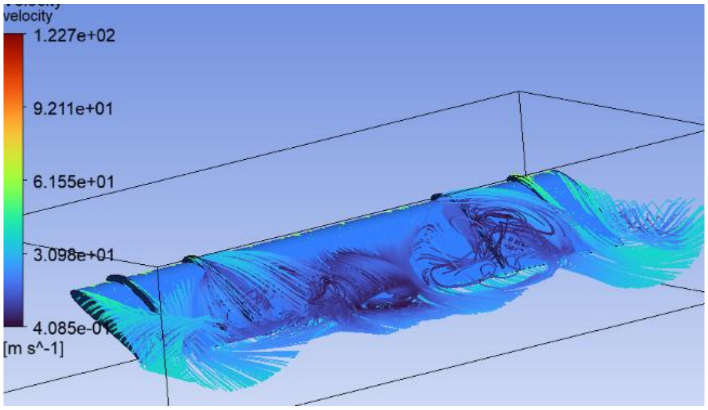

Figure 12: Wing with 4 Wing Fences at Takeoff Conditions and AoA of 25 deg

On the other hand, adding end plates seemed to increase the lift coefficient and move the vortices away from the wing lifting platform like the picture below suggests. The most robust low-speed handling and aerodynamic performance and was therefore selected for further development. These results are consistent with previously reported experimental and numerical studies on flow-control devices for finite wings operating near stall [8,10]. For this reason endplates were considered as a possible fix to the wing tip stall. On the downside it would result in added weight which would be undesirable.

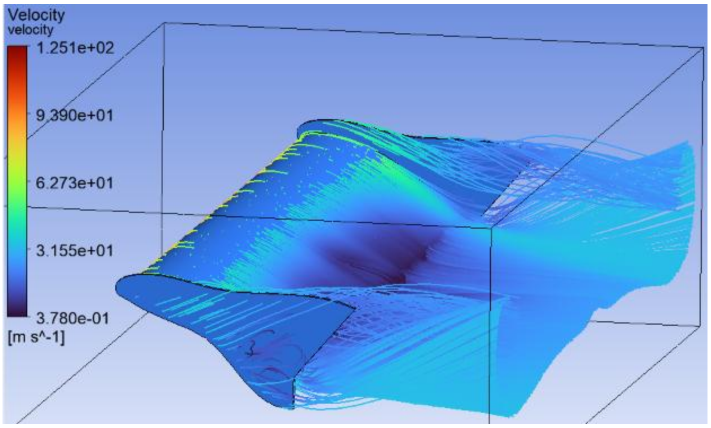

Figure 13: Wing with 2 Endplates at Takeoff Conditions and AoA of 25deg

Another CFD analysis was performed on the wing with props mounted. The purpose of this analysis was to verify the quality of flow over the ailerons at takeoff conditions with an AoA of 10°. This was performed with 14x13 propellers with refined meshes at the wing leading edge, trailing edge and wing tip, and all around the propellers. This resulted in a flow that exhibited conditions satisfying around the aileron's location, furthermore proving a lack of need for wing fences. The CFD for all of these configurations can be viewed in Figs. 12-14.

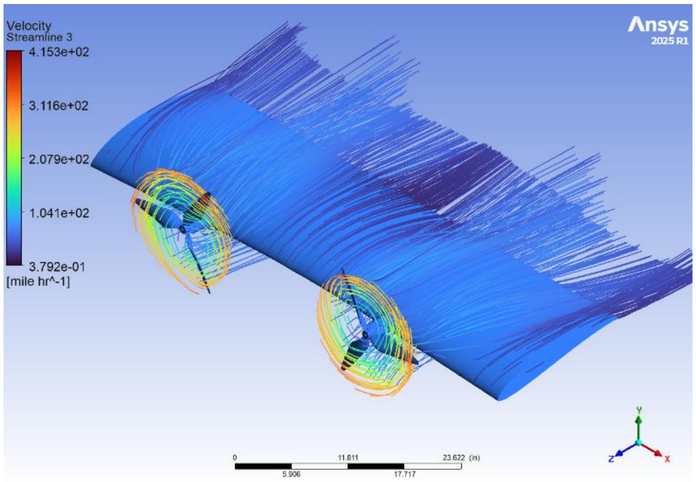

Figure 14: Iteration 1 Wing with propellers at 35mph and 10 deg AoA

The results of the trade study were compiled in table 14 below. It is important to note that despite the promising aerodynamics capabilities of the endplates, the added weight of endplates made it a less desirable solution than the wing tip washout.

Table 14: Aerodynamic Configuration Decision Matrix

Configuration	Δ Lift	Δ Drag	L/D Trend	Flow Behavior	Final Decision
Baseline	Reference	Reference	Reference	Tip separation near stall	Baseline
Wing Fences	−11%	+57%	Significant decrease	Increased separation	Rejected
Endplates	Increased	Slight increase	Improved	Vortex displaced	Rejected

The final CFD simulation was performed on the complete aircraft configuration at a freestream velocity of 60 mph and an angle of attack of 2°. These conditions were selected as conservative trim estimates to verify that the aircraft could generate sufficient lift to meet all mission requirements. The analysis included both propellers operating at full throttle (7300 RPM) in order to capture propwash effects and their interaction with the wing and empennage lifting surfaces.

The simulation predicted a total lift of 24.5 lb and a total drag of 2.2 lb under these conditions. It is expected that actual lift capability will exceed this value in flight, as the selected angle of attack and velocity represents a conservative operating point relative to observed trim conditions. This simulation can be seen in Figure 15.

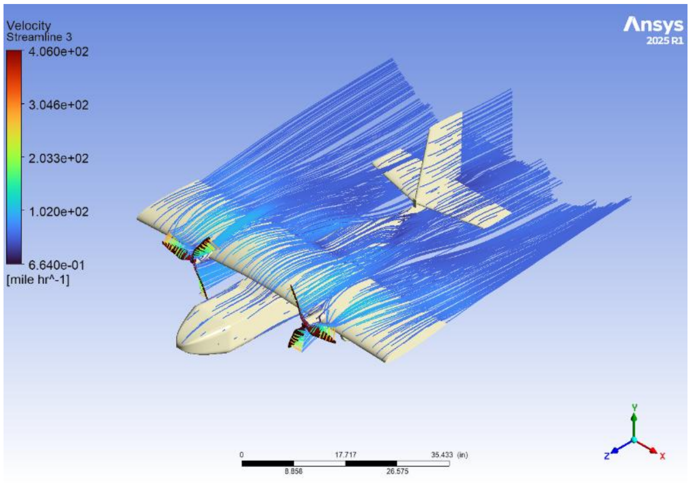

Figure 15: CFD of the entire aircraft at 60mph at 2 degrees AoA

4.3.6 Performance estimation

Using the estimated cruise velocity of 70 mph, the length of the course and the turning radius, estimated used Eqn. (22).

$$R = \frac{V^2}{g\sqrt{n^2 - 1}} \tag{22}$$

$$D_{lap} = D_{straight} + (2 * \pi * R) + (2 * \pi * R) \tag{23}$$

$$T_{lap} = \frac{D_{lap}}{V} \tag{24}$$

Solving for Equation. 22, the turning radius for *Fowl Play* was estimated to be around 120 feet. With this information, Eqns. (23) and (24) were used to get the total distance of 3500 feet and an estimated lap time of 35 seconds, respectively. With these values, it was estimated that the aircraft can ideally complete a total of 17 laps for the missions. Due to external elements such as wind and battery life, a more realistic estimate is 8 to 10 laps for the missions.

4.4 Propulsion System Design

4.4.1 Propeller Sizing

One of the primary constraints in propeller selection was commercial availability, as the DBF competition requires all propulsion components to be commercially sourced. This constraint was further tightened by the selected dual-engine propulsion architecture, which employs counter-rotating propellers and therefore requires manufacturers to offer identical propeller geometries in both clockwise and counterclockwise orientations. Additionally, the aircraft’s payload-driven design and the substantial aerodynamic drag introduced by the banner during Mission 3 necessitated a propulsion system optimized for high static thrust rather than maximum forward speed. As a result, propeller configurations with relatively large diameters and moderate pitch values were emphasized during the selection process.

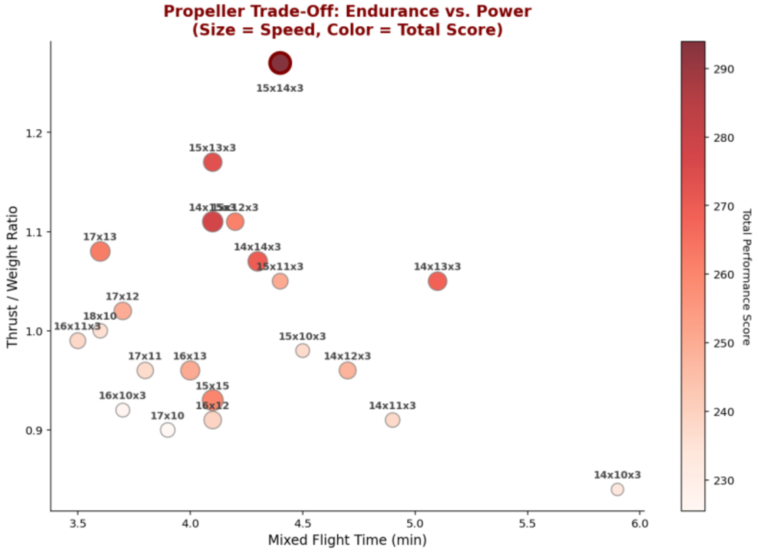

Figure 16: Summary of Propeller Performance Estimated by PropCalc

Propulsion performance was evaluated using the online analysis tool eCalc (also referred to as PropCalc), which enables simulation of propulsion system behavior across a range of propeller diameters, pitches, and blade counts. Key performance metrics considered included static thrust, electrical power consumption, and estimated flight endurance. A summary of the eCalc simulation results is presented in Fig. 16. Based on this analysis, a three-blade 14×13 propeller and a three-blade 15×14 propeller was shortlisted as final candidates, as both configurations provided a favorable balance between thrust capability and flight endurance. Three-blade propellers were selected over two-blade alternatives to achieve the required thrust while reducing overall propeller diameter, thereby improving clearance between the propellers and the fuselage. The selected pitch values were kept sufficiently high to ensure cruise speeds remained well above stall speed across all mission configurations. Both shortlisted propellers were sourced from Master Airscrew and manufactured from fiberglass, offering an appropriate balance of structural stiffness, durability, and weight.

4.4.2 Motor, Battery, and ESC Selection

The selection of a large-diameter propeller necessitates the use of a motor capable of producing high torque at relatively low rotational speeds. Operating a large propeller at high RPM would impose significant aerodynamic and inertial loads on the motor, requiring a physically larger motor and resulting in increased system mass. Conversely, a smaller motor operated at high RPM would draw excessive current, reducing overall efficiency and increasing thermal loading within the propulsion system. To balance these competing constraints, a motor with a low Kv rating and moderate stator size was identified as the most suitable solution. Based on these considerations, the Scorpion SII-4025-520 Kv motor was selected, after several similar candidates were simulated using PropCalc along with the propellers. This motor provides sufficient propulsive capability when paired with either of the shortlisted propellers while remaining relatively lightweight and mitigating thermal risk during high-power operation. Additionally, this motor platform was readily available for testing and had been successfully implemented by the previous design team, reducing integration risk.

The propulsion battery was selected to complement the chosen motor's Kv rating and meet DBF competition constraints. A 4S (four cells in series) lithium-polymer battery, with a nominal voltage of 14.8 V, provides adequate voltage to achieve the required thrust output when paired with the 520 Kv motor. Given the 100 Wh energy limitation specified by DBF rules, the maximum allowable battery capacity was determined by dividing the maximum energy by the nominal battery voltage, yielding a capacity of 6.7 Ah (6700 mAh). Based on commercial availability, the Ovionic 4S-6700mAh battery pack was chosen, both for its compatibility with the selected propulsion system and compliance with competition rules. It maximizes the total allowed propulsive power, it still provides sufficient thrust and endurance, and has a high discharge rating, which allows it to deliver high current for sustained durations while avoiding voltage sagging.

eCalc simulations using the selected motor-propeller-battery combination predicted a maximum current draw of approximately 59 A per motor under peak loading conditions. Based on this result, the Castle Creations Phoenix Edge 75A electronic speed controller (ESC) was selected. The 75A continuous current rating provides a safety margin of approximately 25%, reducing the risk of overheating or ESC failure during sustained high-power operation. Furthermore, the selected ESCs are compact and lightweight, contributing minimally to overall aircraft mass while providing reliable propulsion control.

4.4.3 Finalized Propulsion Configuration

The finalized configuration was once again simulated using eCalc to get performance estimates for the aircraft. The simulation indicated both selected propellers provide sufficient thrust for high payload flight during M2. The estimated thrust in relation to throttle is shown in Fig. 17. The figure compares performance for the two propeller sizes for a twin-engine configuration. Additionally, the propulsion system also incorporates a 100 A blade fuse for arming and safety.

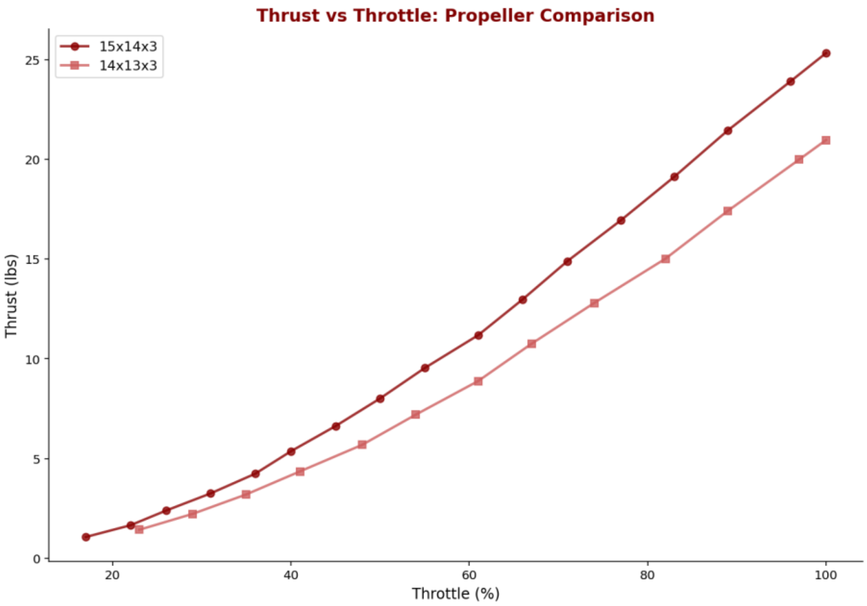

Figure 17: eCalc Estimates for Thrust Progression with Throttle

4.4.4 Controls and Avionics Design

The aircraft control and avionics system follows a simple and robust architecture to ensure reliable manual operation across all mission configurations. All primary control surfaces, including the ailerons, elevator, and rudder, are mechanically actuated by electronic servos through rigid pushrod linkages. This approach minimizes mechanical complexity while providing direct and responsive control authority. An overview of the control system architecture is shown in Fig. 18.

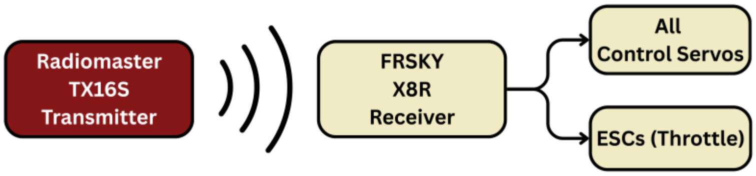

Figure 18: Aircraft Control Architecture

Pilot commands are transmitted from a RadioMaster TX16S transmitter, selected primarily for its availability and flexibility, to an onboard FrSky X8R receiver. The X8R has eight output channels that provide sufficient capacity for all primary flight controls as well as auxiliary systems, along with a smart port that was used for flight telemetry using measurement equipment such as a pitot tube and a voltage sensor for battery monitoring. Channel cross-mapping is utilized where appropriate to allow a single pilot input to command multiple components simultaneously (such as between the rudder and steering), simplifying pilot workload during mission execution.

The receiver distributes control signals to the flight control servos and to the servo-actuated banner deployment and release mechanisms required for Mission 3. To be DBF compliant, the receiver and all avionics components are powered by a dedicated 2S (7.4 V) battery, electrically isolated from the propulsion system. This architecture ensures uninterrupted control authority and overall system reliability. Collectively, the control and avionics design prioritizes simplicity, redundancy, and compliance with DBF competition requirements while supporting safe and repeatable aircraft operation.

4.5 Stability and Handling Considerations

4.5.1. Static Stability and Flying Qualities

To obtain the various stability and control values, the team used the XFLR5 software to design the aircraft, including control surfaces and weights. Simulations were then run at various parameters ranging from optimal cruise to rough, windy takeoff and landing conditions. Fig. 19 below shows the plane set up with the weights for Mission 1.

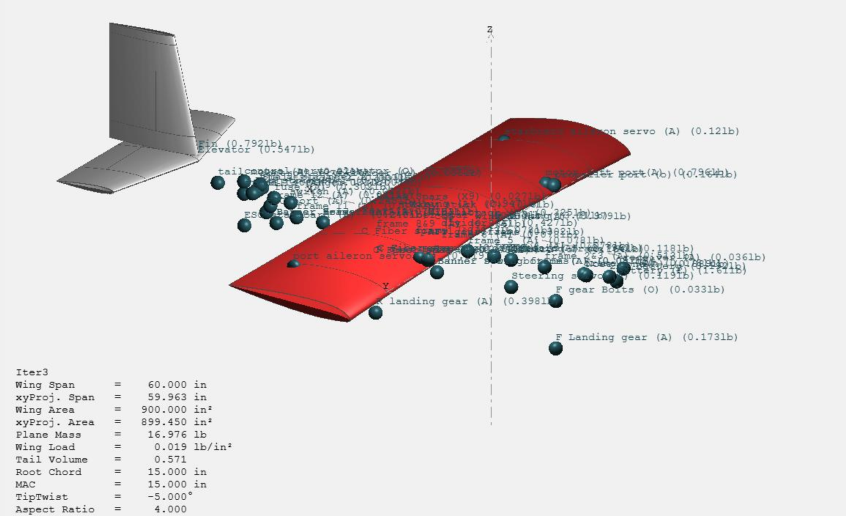

Figure 19: XFLR5 Weight Simulation

To find the aircraft aerodynamic center, XFLR5 static stability simulations were ran with the Center of mass at various locations. Starting from the quarter chord of the wing, the CG was moved further back until the Cm vs Alpha graph showed a linear horizontal pattern showing marginal stability. That point, 30.35 in from the nose cone was determined to be the aerodynamic center.

Fowl Play was designed to exhibit satisfactory longitudinal and lateral static and dynamic stability across all competition mission phases. Aircraft stability characteristics were primarily adjusted through center-of-gravity placement, mass distribution, and wing and tail sizing, allowing the team to balance inherent stability with the maneuverability required for competition performance. Based on established flying-qualities guidelines [13] The static stability derivatives and margins listed in Table 15 were selected to ensure acceptable stability and controllability. These values were used as target ranges during the design and iteration process.

Table 15: Static Stability Data

Mission	Cm_{α}	Cm_{q}	Cl_{β}	Cn_{β}	Cn_{r}	**Static margin**
Suggested values	-0.3 to -1.5	-5 to -30	<0	0.1 to 0.4	-0.1 to -1	10% to 30%
M1	-0.409	-5.500	-0.040	0.171	-0.213	8%
M2	-0.462	-5.570	-0.040	0.171	-0.213	6%
M3	-0.409	-5.500	-0.040	0.171	-0.213	8%

These criteria ensure positive longitudinal static stability, adequate directional stability, and sufficient lateral damping while avoiding overly stiff control responses. The unusual static margin reported for all missions was an adjustment for optimal cruise flights which ensured that the plane would fly at about an AoA of 2° which guaranteed a higher cruise speed and a greater range. Furthermore, this reduction in static margin was a tradeoff for a more controllable aircraft, which was decided after obtaining feedback from the pilot. Apart from static margin, all other criteria were met for all missions.

4.5.2 Dynamic Stability and Flying Qualities

Dynamic stability requirements were selected based on handling-quality Levels 1–3 (L1-3), as summarized in Table 16. These criteria guided the sizing of control surfaces and the distribution of mass to achieve acceptable transient responses in roll, spiral, Dutch roll, short-period, and phugoid modes.

Table 16: Dynamic Stability Data

Flying Levels	Roll	Spiral	Dutch Roll	Short Period	Phugoid
L1	$\tau < 1.0$ s	$t2 > 12$ s	$\zeta > 0.19$ | $\omega n > 1.0$ | $\zeta\omega n > 0.35$	$0.35 < \zeta < 1.30$	$\zeta > 0.04$
L2	$\tau < 1.4$ s	$t2 > 8$ s	$\zeta > 0.02$| $\omega n > 0.4$ | $\zeta\omega n > 0.05$	$0.25 < \zeta < 2.0$	$\zeta > 0.02$
L3	$\tau < 10.0$ s	$t2 > 4$ s	$\zeta > 0$ | $\omega n > 0.4$	$\zeta > 0.15$	$T2 > 55$ s

The various designs under all conditions met at least handling qualities of level 2, which were determined to be satisfactory for the flight conditions, showing stable behaviors. The only outlier was the spiral mode, which showed instability under high sideslip recovery at low speed and high AoA. Those conditions were acknowledged but did not disqualify the design, especially given that the time to diverge in those conditions was still above 15 seconds, ensuring flying qualities of level 3 in the worst conditions. Note that this issue is set to be addressed by using a vertical strake in front of the vertical tail to keep the Rudder flying at high sideslip angles.

4.5.3. Handling Qualities

Given the gusty wind conditions typical of Wichita, Kansas, the team intentionally opted for a highly maneuverable aircraft capable of rapid attitude corrections and precise control inputs. This design approach prioritized responsive roll and yaw performances and adequate damping to mitigate disturbances while maintaining stability margins within acceptable limits. The resulting closed-loop stability characteristics are shown in Fig. 20, which presents the root locus of both the lateral and longitudinal responses under near-stall, windy conditions for Mission 1. Through iterative flight testing and pilot feedback following the initial test flights, handling-quality criteria were refined to improve controllability and pilot workload. These refinements directly informed adjustments to control surface sizing and CG placement, resulting in improved overall performance under realistic competition conditions. One of the major refinements was the increase of control surfaces on the tail to gain approximately 1 ° of trim per control surface deflection.

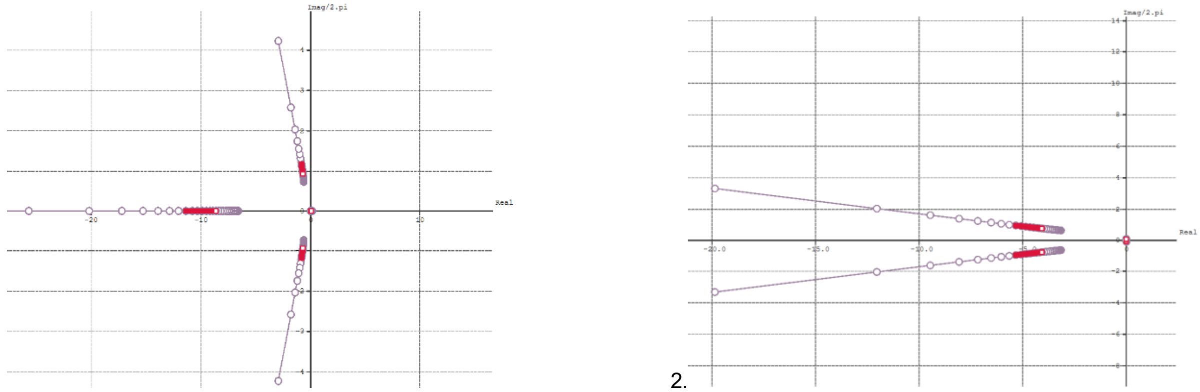

1.

2.

Figure 20: Root Locus of Lateral (1) and Longitudinal (2) Response of the System in Mission 1 Under Windy Conditions Near Stall with Different Control Parameters

5.0 Detail Design

Following completion of the conceptual design and preliminary design phases, the detailed design phase focused on refined analysis, validation testing, and subsystem optimization through both ground and flight testing. Emphasis was placed on mass reduction, manufacturability, and structural integrity to ensure the aircraft could reliably support the mission-required payload while maintaining aerodynamic and performance targets.

5.1 Dimensional Parameters

The finalized dimensional and configuration parameters resulting from this phase are summarized in Table 17, including wing and tail geometry, fuselage dimensions, and propulsion system selections. These parameters reflect the balance achieved between aerodynamic efficiency, structural capability, and mission adaptability.

Table 17: Dimensional Design Parameters

Wing		Horizontal Tail	
Airfoil	Eppler 398	Airfoil	NACA 0010
Span (ft)	5	Span (ft)	2.4
MAC (ft)	1.5	Chord (ft)	0.833
Planform Area (ft^2)	7.5	AR	2.88
AR	3.333	Planform Area (ft^2)	2
Incidence Angle (°)	0	Incidence Angle (°)	-2
Washout(°)	5	Tail Arm (ft)	2.5
Fuselage		**Vertical Tail**	
Length (ft)	4.5	Airfoil	NACA 0010
Width (ft)	0.75	Span (ft)	1.023
Height (ft)	0.5	Chord (ft)	0.917
Propulsion		AR	1.115
Receiver	FrSky X8R	Planform Area (ft^2)	0.937
Motor	Scorpion SII-4025-520	Incidence Angle (°)	0
Propulsion Battery	4S 6700mAh	Tail Arm (ft)	32
Avionics Battery	2S 1500mAh	**Propeller**	
ESC	CC Phoenix Edge 75A	M 1/2/3	14x13x3

5.2. Structural Analysis

5.2.1 Wing Structure

Following the conceptual and preliminary design phases, a more detailed design was conducted with additional analysis. This process incorporated the expected flight conditions (notably a maximum bank angle of 75°) and the preliminary results, providing the load factor from mission analyses. The limits were computed using a safety factor of 1.5. The resulting V-n diagram is shown in Fig. 21. Therefore, each aircraft component was designed in accordance with the constraints defined by this diagram.

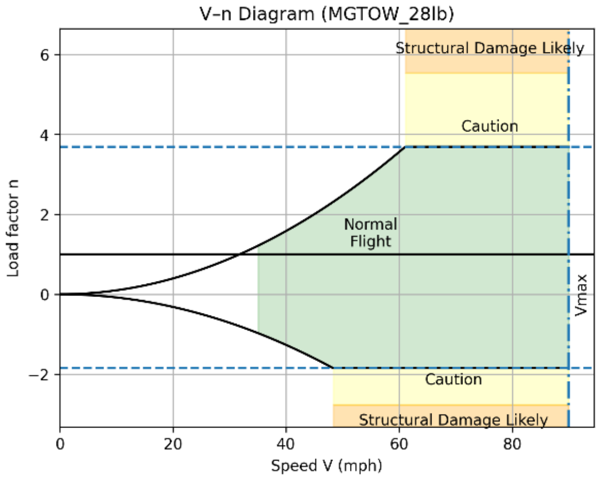

Figure 21: Fowl Play VN diagram

The wing is primarily supported by a vertical “sandwich” spar, comprising of a layer of Nomex honeycomb between two carbon fiber layups. This spar is bolted into the 3D printed wing mount, which is bolted into mounts within the fuselage. The balsa wood airfoils are mounted on this spar using 3D printed mounts, while the 3D printed airfoils are superglued directly onto the spar. This configuration was selected to maximize structural strength while also serving as the primary load path between the wing and fuselage. This minimizes weight of the load bearing components of the wing by relying on a lightweight combination of composite material and superglue. This cross-sectional view is shown in Fig. 22, while Fig. 23 shows the cross-sectional view of the wing at the ailerons, which include a 3D printed trailing edge.

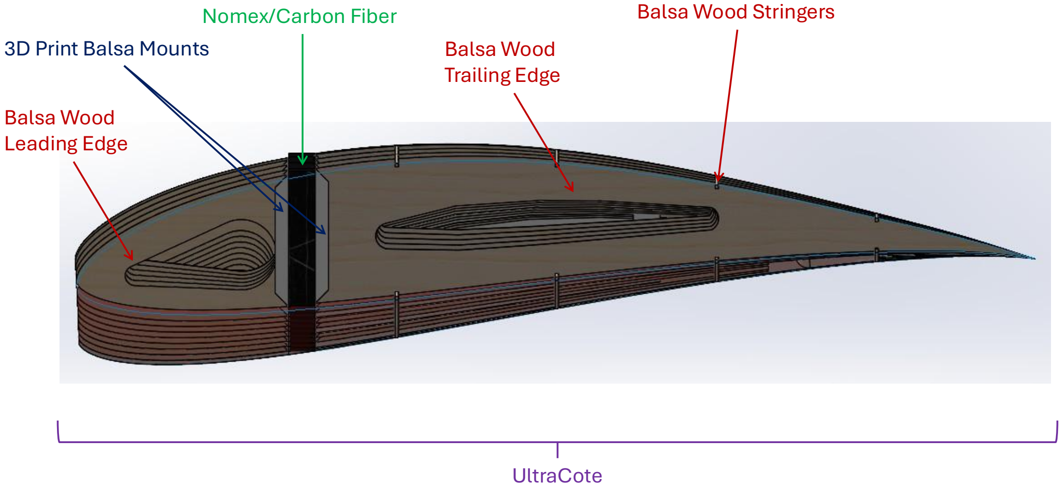

Figure 22: Wing Cross-Section Material Layout

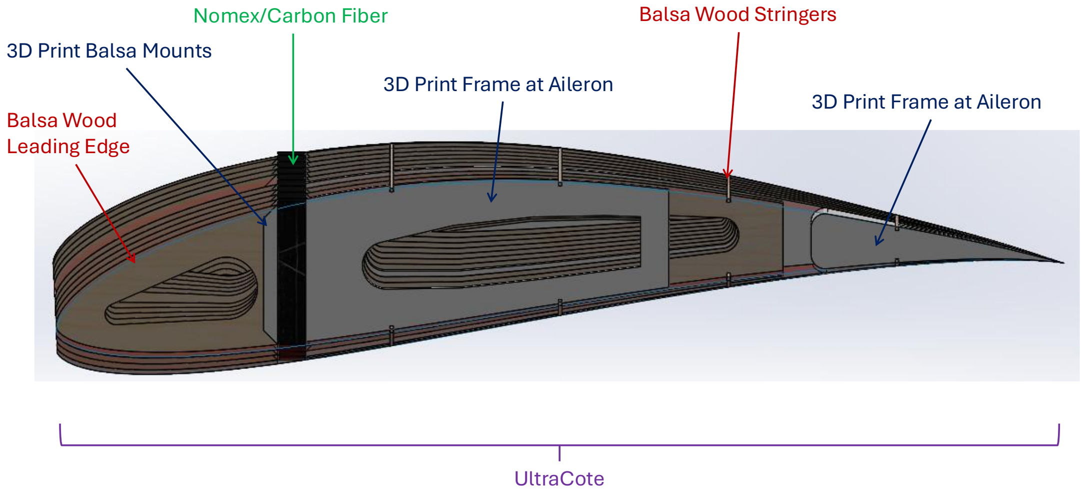

Figure 23: Wing Cross Section at Aileron Material Layout

The wing geometry was formed using 1/8 in. balsa wood ribs spaced at two-inch increments along the wingspan at the leading edge. These ribs were individually designed with internal cutouts for weight reduction, attachment points for the spar, and to provide a wing twist about the trailing edge such that each rib coincided with the spar at unique angles. The ribs were laser cut and bonded to the main spar and lower wing surface. The ailerons and the ribs supporting them were additively manufactured using PETG to ensure structural integrity during flight. All ribs were connected using balsa wood stringers, after which an Ultrakote skin was applied to the surface of the wing to protect the internal components and provide a smooth aerodynamic surface, seen in Fig. 24.

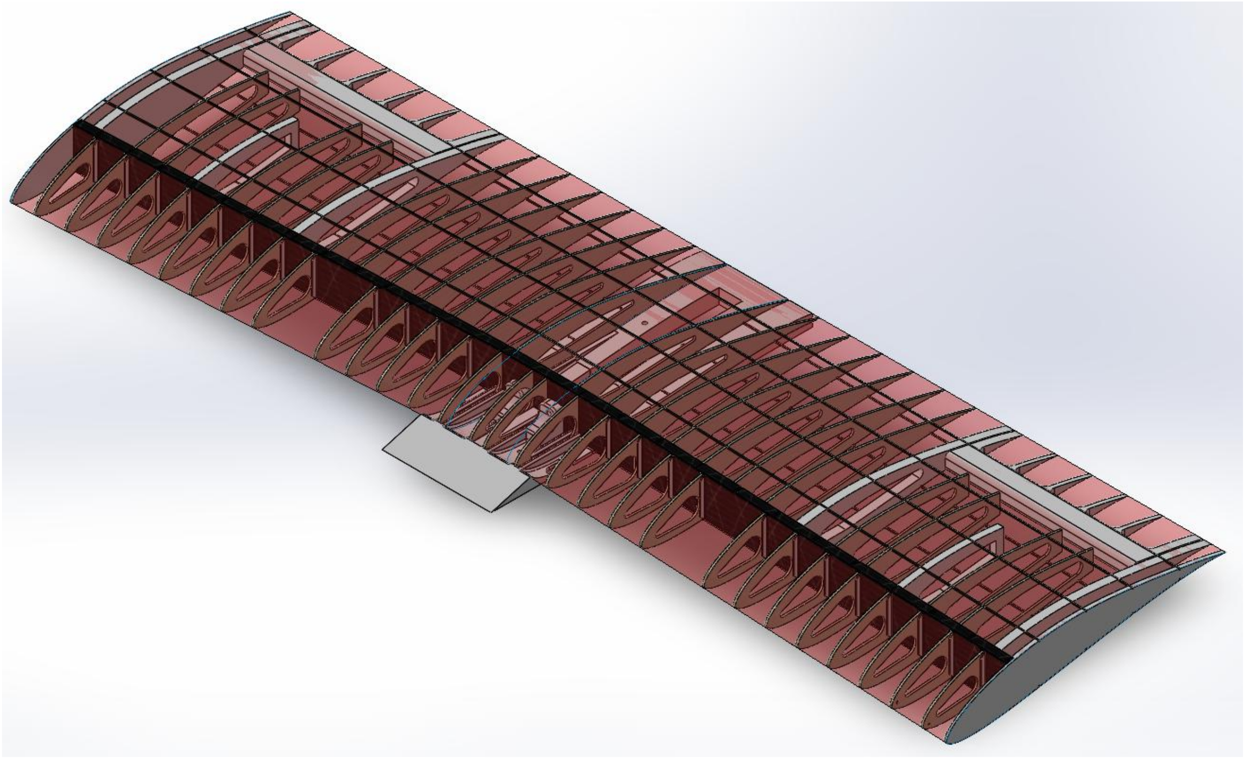

Figure 24: Aircraft Wing Structural Assembly

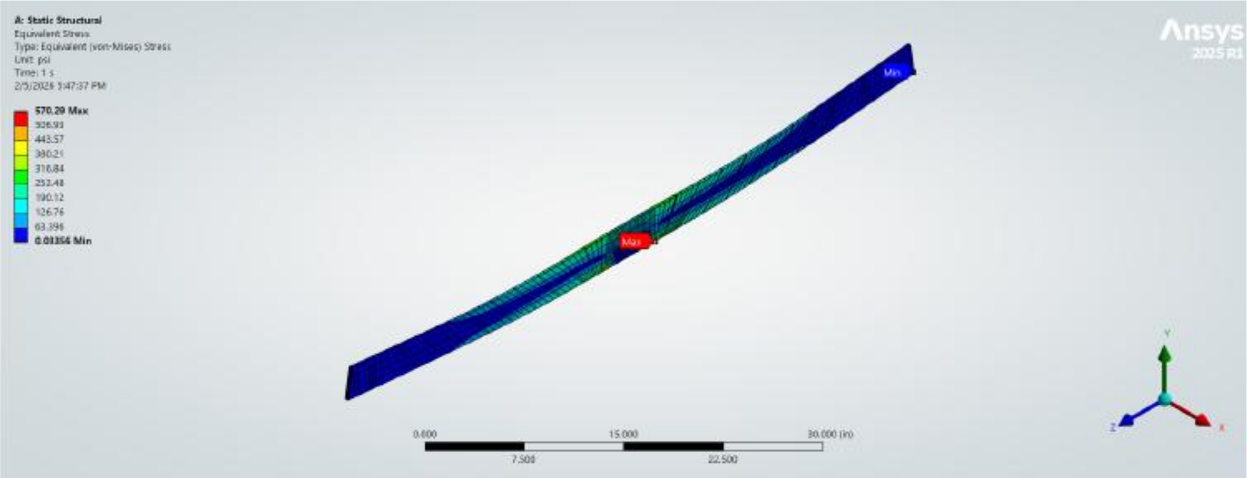

Figure 25: Wing Spar Stress Analysis Under 25 lb load

FEA of the wing spar was conducted in Fig. 25 to account for the mass of the fully loaded plane under normal flight conditions. The conditions were set by applying an even, upwards, shearing 25 lb force across the front and back faces of the spar, where the airfoils are mounted. The resistance comes from the clamped section of the spar where it is mounted to the fuselage of the aircraft. The maximum stress comes out to be over 570 psi, which the structure can easily handle, having a safety factor greater than 15. The upwards flex is a result of the deflection caused by the force, which ANSYS magnifies for visibility.

5.2.2 Fuselage & Tail

The fuselage design consists of a series of structural frames, with approximately eleven frames defining the payload volume and an additional two frames used to taper the empennage. Two of the frames are connected and act as the supporting frames for the front landing gear. There is an additional rear landing gear attachment and two internal wing mounts mounted on the spars. All frames and mounts were printed using PETG. The nose cone is connected using hinges on the first frame and the tail by a PETG printed hockey mount. A carbon fiber hockey stick runs longitudinally through cutouts in each frame and acts as the primary structural member connecting the fuselage and empennage frames. Additional balsa wood stringers are installed externally along the fuselage to provide shaping of the skin and internal carbon fiber spars to provide secondary structural support. Ultrakote material is used as the exterior skin of the fuselage to minimize structural weight while reducing the use of more costly carbon fiber material. The final fuselage configuration is shown in Fig. 26.

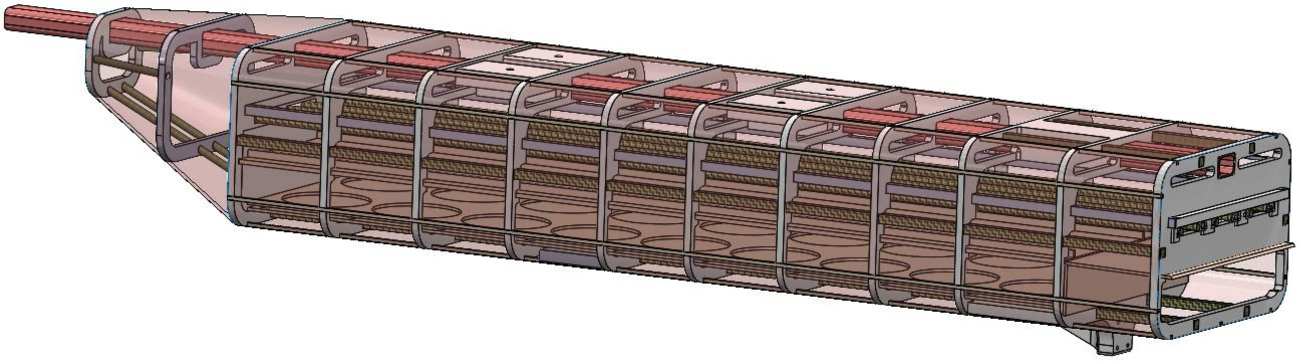

Figure 26: Aircraft Fuselage Structural Assembly

5.2.3 Tail Structure

The horizontal stabilizer consists of 18 ribs, each 1/8 in thick, with two endcap ribs to ensure structural stability. 8 of the internal ribs are made of balsa wood, with the rest being made of PETG. The elevator was additively manufactured using ASA Aero. The ribs were connected using a square carbon fiber spar in the front, and another in the middle, along with a circular carbon fiber spar through the back. The circular spar acted as the axis of rotation for the elevator, and stringers along the top and bottom of the ribs were added to maintain airfoil shape. Ultrakote was applied to ensure a smooth aerodynamic surface. The vertical stabilizer was manufactured in a similar fashion, consisting of 9, 1/8 in. thick ribs, with an endcap rib on the top to ensure structural stability. 4 of the ribs are made of balsa wood, with the rest of the ribs being made of PETG. The rudder was additively manufactured using ASA Aero. Like the horizontal stabilizer, the vertical stabilizer also uses two square carbon fiber spars to hold the ribs together, with a circular spar running through the back and acting as the rotational axis for the elevator. The construction is finished by adding balsa wood stringers and Ultrakote. The vertical and horizontal stabilizers were connected to a mount made from PETG, which is attached to the end of the hockey stick on the fuselage. The vertical strake, which is made out of balsa and carbon fiber, is mounted in the middle of the tail mount, along the top of the last two fuselage frames and the face of the tail mount that extends to the fuselage. This configuration can be seen in Fig. 27 below.

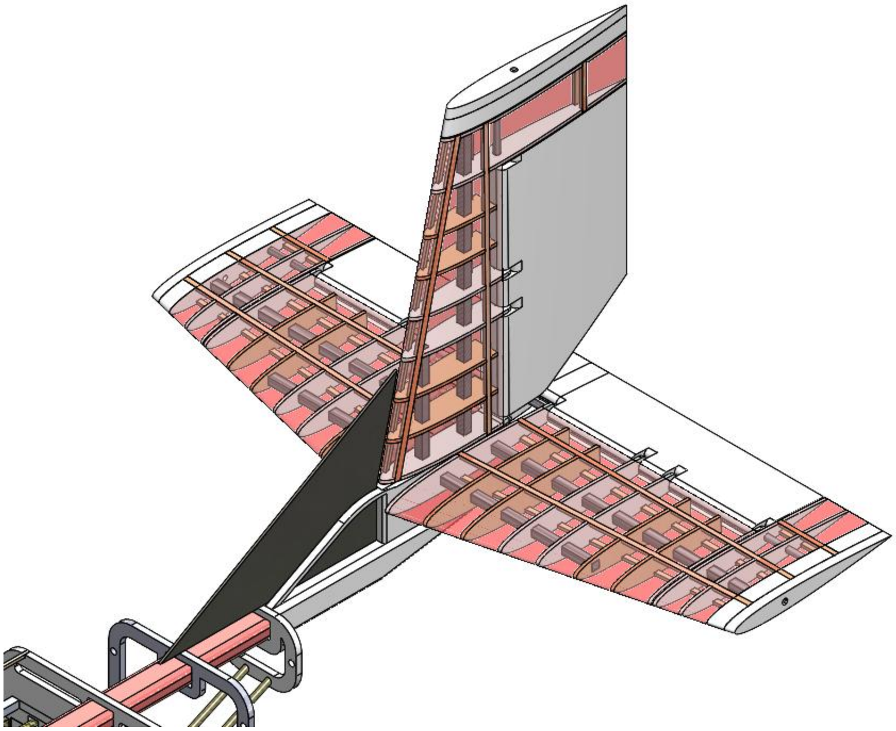

Figure 27: Aircraft Tail Structural Assembly

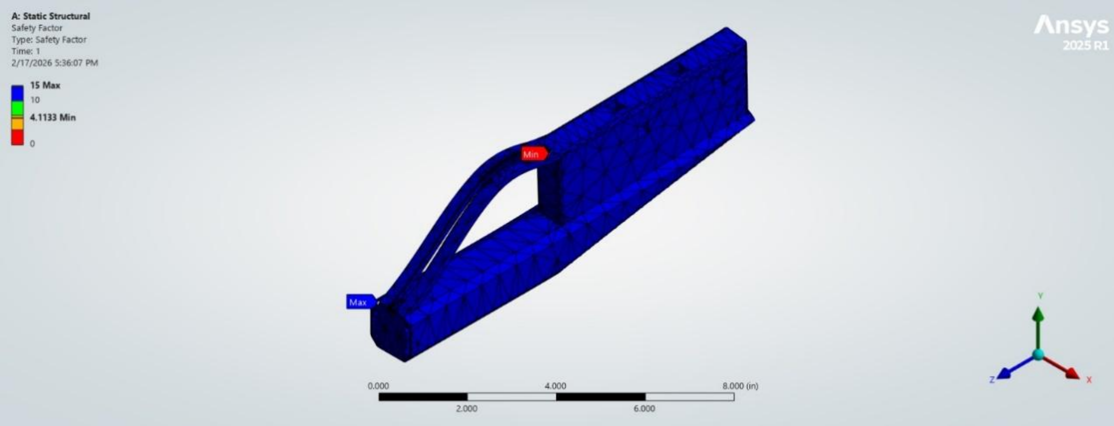

Figure 28: Tail Mount Structural Analysis Under High Deflection

Fig. 28 above shows the FEA of the tail mount structure, conducted assuming an extreme deflection case in both the elevator and the rudder. The simulation was run with an upwards elevator force of 18.7 lbs and a rightward rudder force of 10.6 lbs. The drag estimated was 3.59 lbs on the horizontal stabilizer and 2.26 lbs on the vertical stabilizer. Under this case, which had a maximum stress of 1849 psi, the PETG plastic is expected to hold steady, maintaining a safety factor greater than 4.

5.2.4 Landing Gear Design

The landing gear system securely latches to aircraft to optimize ground maneuverability and stability. A carbon fiber rear landing gear was selected to have a width of 25% of the wingspan, equaling 15 inches, while minimizing the height to lower the center of gravity. The front landing gear consists of an aluminum rod that is latched vertically while being allowed to rotate. This part is steered by a servo mounted just behind the landing gear.

Both the front and rear landing gears have 3D printed PETG attachments. The front landing gear attachment is made by combining two reinforced modifications of the aircraft's ribs, leaving screw holes that allow for mounting. The part has another 3D printed connector that attaches to the frame using screws, allowing for quick repairs, tweaks, and customizability. The rear landing gear attachment is mounted on 2 spars on the bottom of the aircraft. The landing gear itself is directly screwed in via drilled holes created in the part, with a small metal plate sandwiched between for shock absorption and even force distribution. The front gear itself is made from a 0.25" diameter aluminum rod sanded at the end to fit smaller 3" tires. The rod was bent into an S-like shape with a vertical top section to allow for ease of mounting and rotation. The assemblies can be seen in Fig. 29 and 30.

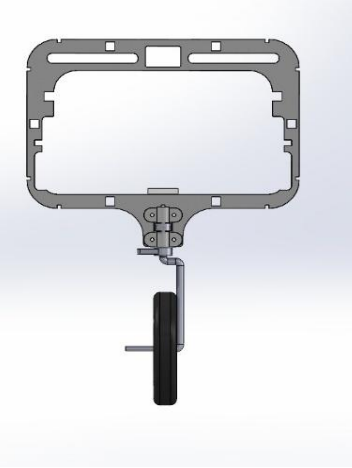

Figure 29: Front Landing Gear Assembly

Figure 30: Front Landing Gear Assembly

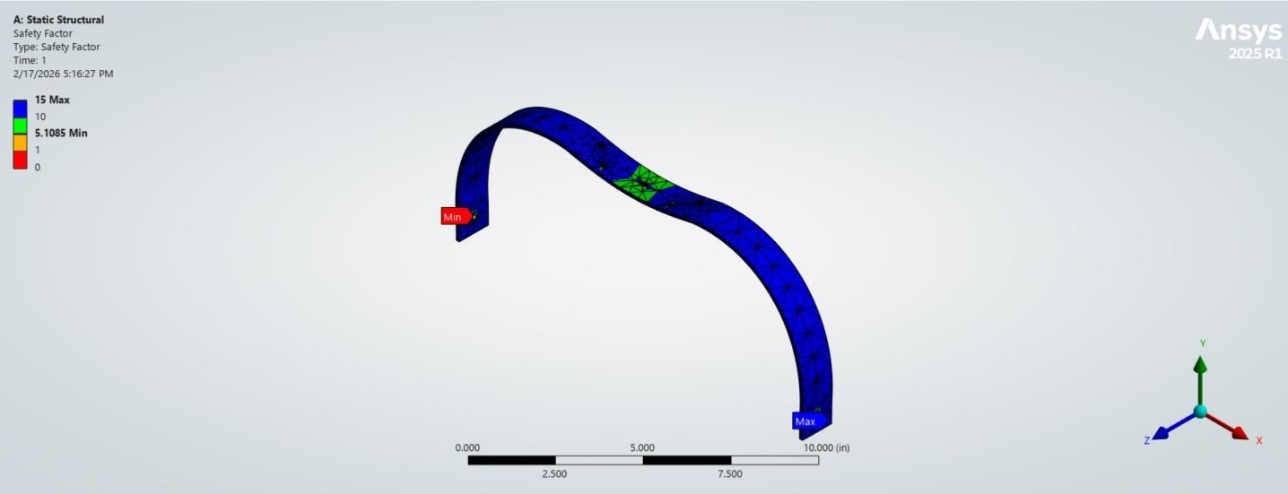

Figure 31: Rear Landing Gear Structural Analysis Under 30lb Load

The Rear Landing Gear's FEA was conducted in Fig. 31 to test an impulse of 30lbs. Due to the small area of the tire axle within the part, high forces get concentrated in that small area, leaving a safety factor of just over 5 and experiencing a stress of up to 15337 psi. The flexing seen in the part shows that this part will be effective at softening these impacts and tolerating the forces it will undergo.

5.2.5 Passenger and Cargo Mounting

The passengers will be supported at the neck by two carbon fiber rods running longitudinally along the fuselage. The aircraft is designed to accommodate three rows of passengers, with each row capable of holding approximately 16 passengers for a total capacity of 48 ducks. A 3D printed duck removal system is incorporated to allow efficient unloading. This system enables passengers to be extracted in groups of three and pulled forward to the nose cone for simple removal.

The carbon fiber support rods are secured to a structural frame at the rear of the aircraft and constrained at the front using springs. During loading, the rods are spread apart at the nose just enough to allow each passenger's head to pass between the rods. The loader then pushes the passenger rearward to the farthest reachable position and repeats the process until the row is filled. For unloading, the first three passengers at the nose are manually removed. The removal system is then used to pull the next set of three passengers forward for extraction. The fastening approach reduces the weight associated with a more complex constraint mechanism and minimizes the unused internal volume. By optimizing this, the fuselage cross section can be reduced, reducing weight and aerodynamic drag.

Cargo will be stored beneath the passenger compartment in a sliding tray assembly. This system consists of two trays joined together with spacers and construction from balsa wood and carboard to minimize weight. The tray is designed to slide outward to expedite loading and unloading, but it cannot be completely removed from the aircraft. The passenger and cargo compartments are separated by a thin carboard divider on which the ducks sit.

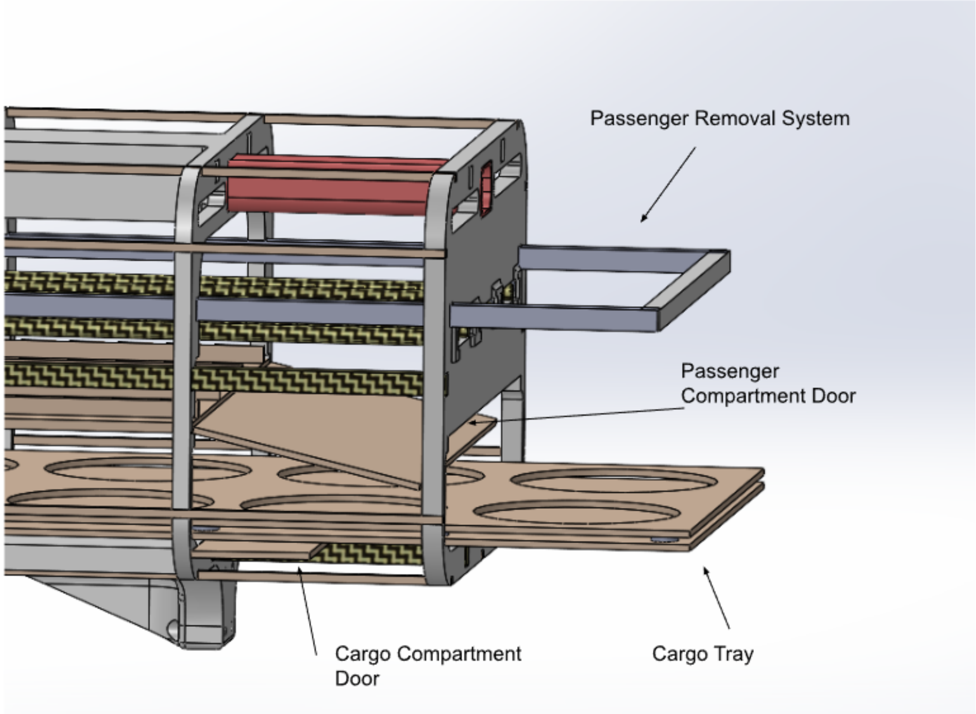

Figure 32: Cargo & Passenger Configuration

Both the passenger and cargo compartments have independent access doors. The passenger compartment door is parallel to the passenger tray and hinges downward to allow for efficient passenger loading. This provides direct access to carbon fiber support rods, to allow for efficient loading and unloading of passengers. The cargo compartment door is perpendicular to the cargo tray and hinges downward. This allows the sliding tray to extend outward for loading and unloading of cargo. The carbon fiber rods are originally in compression using springs that are fixed to the first structural frame as seen below. These springs provide forward constraints while allowing deflection during passenger insertion and removal.

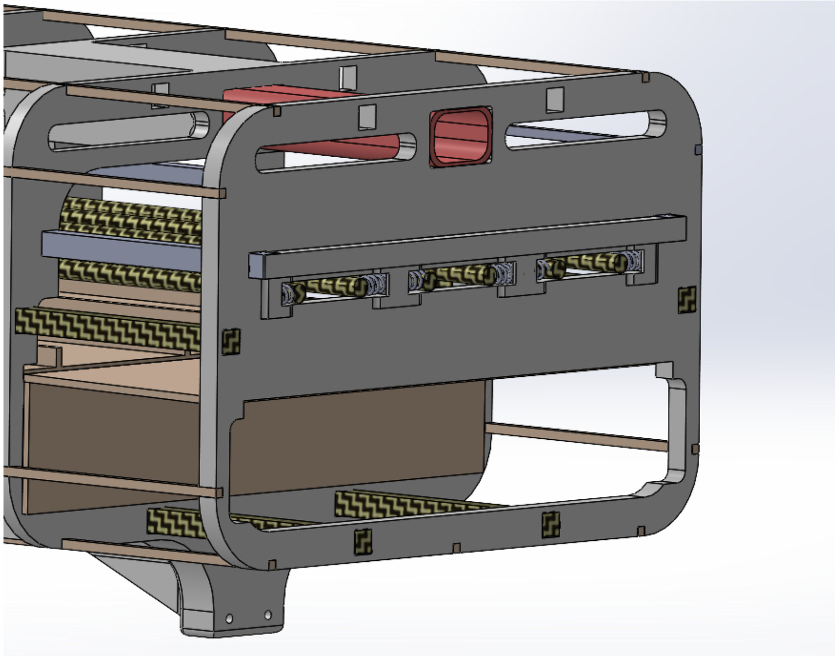

Figure 33: Fuselage Loading Configuration

5.3 Avionics and Wiring

The finalized propulsion and control systems are electrically integrated according to the wiring architecture shown in Fig. 34. The propulsion system consists of a twin-engine configuration, including the propellers, motors, ESCs, main propulsion batteries, and a mechanical arming fuse. The flight-control system includes two aileron servos, one rudder servo, one elevator servo, and two servos dedicated to the banner deployment and release mechanisms. A single receiver is shared between the propulsion and avionics systems, distributing control signals to all actuated components. To improve system robustness, the receiver and all avionics are powered by a dedicated battery, electrically isolated from the propulsion power system.

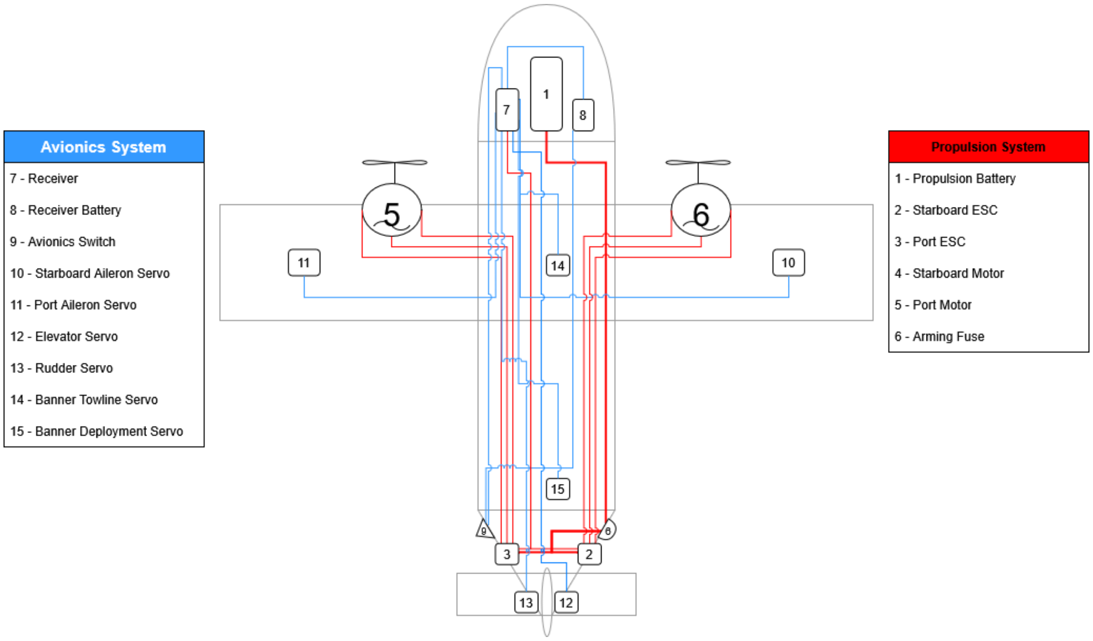

Figure 34: Wiring Diagram for the Aircraft

The control surface servos were chosen by calculating the required torques for each control surface at maximum deflection, using the formula below. Appropriate commercially available servos that provided sufficient torques with acceptable safety margins were then selected for the primary avionics, calculated using Eq. (23).

$$\text{Torque (oz-in)} = 8.5 \times 10^{-6} \times \left(C^2 V^2 L \frac{\sin(S1)\tan(S1)}{\tan(S2)} \right) \tag{23}$$

where, C is control surface chord in cm, L is control surface span in cm, V is speed in mph, $S1$ is the max control surface deflection in degrees, and $S2$ is max servo deflection in degrees.

5.3.1 Motor and ESC Mounting Interface

The two motors are mounted on the leading edge of the wing and attached to the vertical carbon fiber sandwich spar. The mounting interface incorporates a 3D-printed spacer, ensuring that the propeller plane is positioned forward of the leading edge. This placement prevents damage to both the wing and the propeller during operation. The motor and spacer interface, as well as its placement on the wing's vertical spar, are shown in Fig. 35 below.

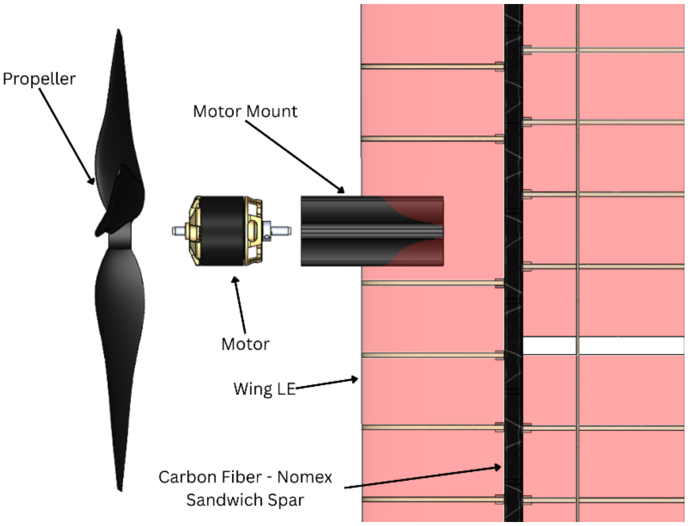

Figure 35: Top view of Motor Mounting Interface on Wing

Conversely, the ESC mount features a 3D-printed heat sink design utilizing a lattice structure to enable passive thermal management. This design dissipates heat without requiring direct airflow over the ESC, effectively preventing the ESCs from overheating during flight while also avoiding additional drag from an external ESC mount. The mount is located on the outer walls of the fuselage at the rear of the aircraft, as shown in Fig. 36 below.

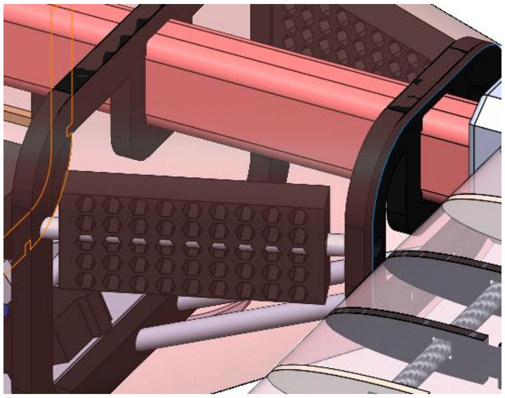

Figure 36: ESC Mounting Interface at the Rear of the Aircraft

5.3.2 Banner Subsystem Design

The banner attachment point is placed at the aircraft's aerodynamic center (AC) to minimize the pitching moments that occur when the banner generates drag. Attaching the load at the center of gravity (CG) or farther aft would introduce a significant nose-up pitching moment as the banner pulls backward, forcing the control surfaces to work harder to maintain level flight and reducing overall stability. By anchoring the banner at the AC, where changes in aerodynamic forces produce minimal rotational effect, we ensure that the aircraft experiences primarily a straight, rearward pull rather than a torque. The banner attachment point can be seen in Fig. 37.

Nylon ripstop was chosen as the banner material because it had the best balance of strength, weight, and cost among the common options. It was chosen over vinyl, polypropylene, and polyester since it was the most viable material for our purposes. With a Young's modulus of about 3000 MPa, and a mass of 1.2 oz/yd^2, ripstop ensured the banner could be structurally stable without creating excess drag or weight. The banner will be straightened with a carbon fiber rod attached to the leading edge, with sewn-in weights on the bottom end to ensure verticality. The trailing edge of the banner will have double-sewn material to increase stiffness and reduce flapping.

The banner deployment and release feature a two-stage mechanism. The first stage is to deploy the banner in a vertical configuration behind the aircraft such that any text on the banner appears upright. After completing as many laps as possible within a 5-minute window, while towing the banner, the next stage is to completely detach the banner from the plane.

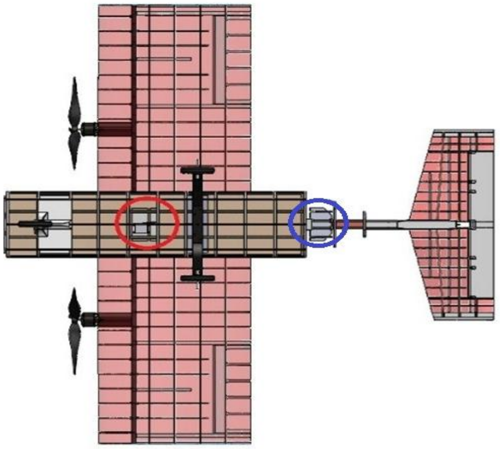

Figure 37: Banner Attachment Point Circled in Red, Deployment Point Circled in Blue

The subsystem design hence features two servo-actuated mechanisms for banner deployment and release, as shown in Figs. 38(a) and 38(b). The deployment mechanism shown includes two 3D printed hooks connected to a shaft, which then connects to a servo. The servo actuation allows the hooks to open or close, allowing the banner to be stowed. The stowing mechanism requires the banner to be rolled around a solid rod at the leading edge of the banner, which also allows it to stay upright after deployment. This mechanism is located at the aft of the aircraft, in the tapered section of the fuselage.

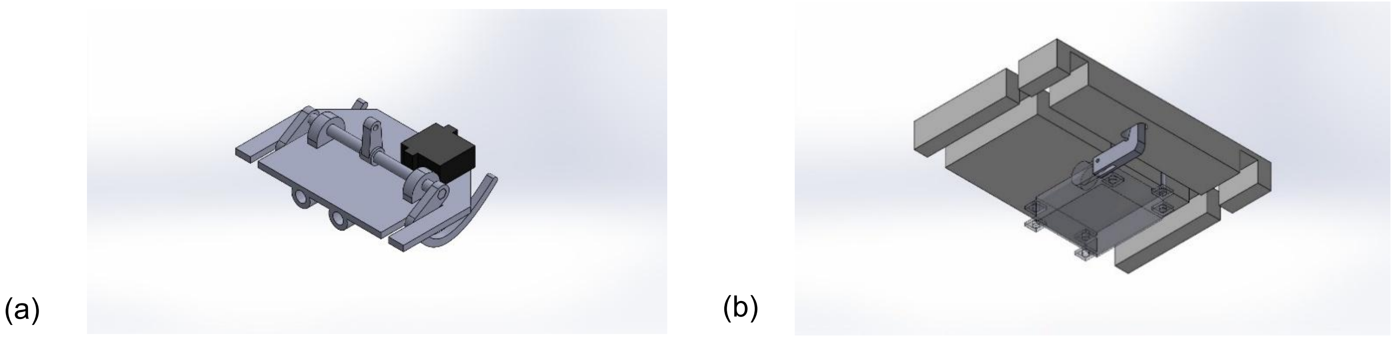

(a)

(b)

Figure 38: CAD Model of Banner Deployment (Left) and Release (Right) Mechanisms

The release mechanism includes a simple hook attached directly to a servo arm, which allows the hook to move in and out of a slot/hole. The hook keeps the banner towline attached to the aircraft while in the closed position (figure above shows the closed position), and when opened, the drag experienced by the banner allows the towline to be released and pulled away from the aircraft. The slot, which is the point of attachment for the towline, is located exactly at the AC of the aircraft, which minimizes the moments experienced by the aircraft due to the banner drag during flight.

5.4 Weight & Balance

Building upon a preliminary weight table of OU DBF previous year's components, each component's weight was updated as the various parts were purchased or manufactured. Upon every subassembly, a weight and moment check was operated to check for mismatch and adjust for errors that may have occurred. The position of components was determined from the aerodynamic team requirements, mission constraints and from manufacturing limitations. For components with less restrictions on placement, positioning was based on locations that would create the least moment about the wing quarter chord point which was the first estimate of aerodynamic center location. Hence the components weights were recorded and moments calculated using the nose cone tip as a reference point. The results were gathered in table 18 and 19 below, showing all components accounted for, and each mission CG sheet with their X and Z location with respect to the nose cone tip and top of the fuselage.

Table 18: Weight and Balance Breakdown of Fowl Play

LE 21 in from datum	Weight (lbf)	X position	Z position	X moment	Z moment
STRUCTURES	**12.027**			**353.217**	**-11.346**
Rear Landing Gear	0.398	33.750	-11.980	13.423	-4.765
Rear Gear Bolts	0.022	33.750	-6.600	0.743	-0.145
Front Landing Gear	0.173	11.500	-11.980	1.985	-2.068
Front Gear Bolts	0.033	11.500	-6.600	0.380	-0.218
Fuselage	2.595	25.609	-3.437	66.446	-8.902
Empennage	0.384	50.457	-1.646	19.389	-0.578
Horizontal Stabilizer	0.906	57.716	1.085	52.292	0.263
Vertical Stabilizer	0.536	57.641	8.036	30.883	1.151
Main Wing	3.106	28.770	0.939	89.373	2.917
Wing Mount	0.979	14.200	0.000	13.899	0.000
Nose Cone	0.889	7.720	-3.000	6.864	-3.582
Hockey Stick	0.600	32.000	-0.375	19.200	-0.225
Miscellaneous	1.407	27.250	0.000	38.341	0.000
PROPULSION	**6.116**			**124.451**	**-6.996**
ESC Port	0.248	48.600	-4.000	12.054	-0.992
ESC Starboard	0.248	48.600	-4.000	12.054	-0.992
Port Motor	0.796	20.500	0.870	16.324	0.693
Starboard Motor	0.796	20.500	0.870	16.324	0.693
Port Propeller	0.164	18.500	0.870	3.030	0.143
Starboard Propeller	0.164	18.500	0.870	3.030	0.143
Switch	0.022	46.000	-2.630	1.012	-0.058
Port Aileron Servo -Wing	0.119	28.850	0.870	3.422	0.103
Starboard Aileron Servo - Wing	0.120	28.850	0.870	3.460	0.104
Fuse	0.302	46.000	-1.000	13.873	-0.302
Propulsion Battery	1.606	3.500	-3.000	5.621	-4.818
Avionics Battery	0.192	3.500	-2.000	0.674	-0.385
Control Servo - Elevator	0.035	52.500	0.000	1.852	0.000
Control Servo - Rudder	0.035	54.500	0.000	1.922	0.000
Banner Servo Back	0.031	46.000	-4.000	1.420	-0.123
Banner Servo Bottom	0.057	26.160	-6.000	1.491	0.000
Receiver	0.036	3.500	-2.000	0.125	-0.071
Wiring	0.947	24.500	0.000	23.204	0.000
Steering Servo	0.119	17.000	-6.000	2.016	-0.712
MISSION 1 SPECIFIC	**0.680**	**3.000**		**2.040**	**-5.444**
Counterweight	0.680	3.000	-0.800	2.040	-5.444
MISSION 2 SPECIFIC	**8.651**	**19.500**		**219.582**	**-16.254**
Ducks	2.230	26.450	-3.635	58.984	-8.106
Pucks	6.370	25.000	-1.250	159.250	-7.963
Duck Pins	0.051	26.450	-3.635	1.349	-0.185
MISSION 3 SPECIFIC	**0.695**				
Banner	0.015	46.000	-5.000	0.710	-0.077
Deployed	0.015	76.160	-5.000	1.175	-0.077
Counterweight	0.680	3.000	-0.800	2.040	-5.444

Table 19: Total Missions Weights, Center of Gravity Location Along x axis and SM as % of MAC

Mission	GTOW (lbf)	X CG from Datum (in)	SM as % of MAC
M1	18.824	26.314	8%
M2	26.794	26.711	6%
M3.1	18.839	26.315	8%
M3.2	18.839	26.625	7%

The different mission weights were plotted versus the center of mass location and located on the center of gravity envelope developed based on the aerodynamic position and the acceptable limits. Fig. 39 allows for a better understanding of how much margin there is for the coming iteration, and eventually how much weight needs to be reduced.

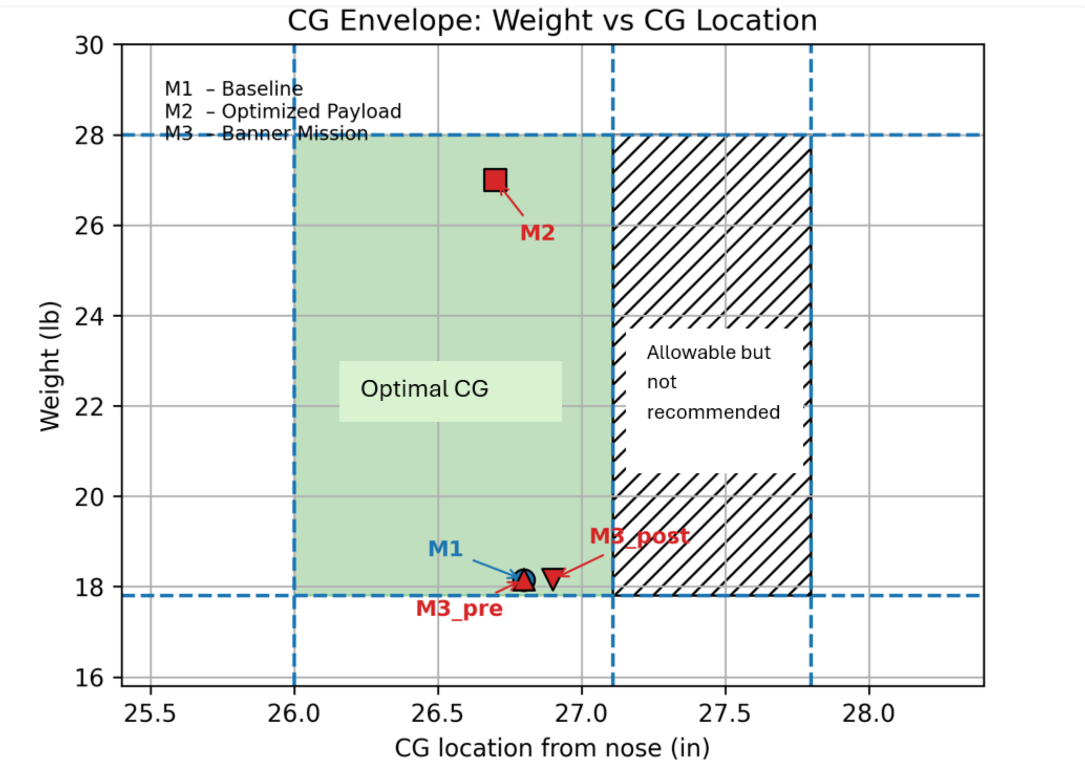

Figure 39: Mission Weights Plotted Versus their CG Positions

5.5 Mission Performance

The table below shows Fowl Play's performance values with respect to each mission of interest for the DBF competition. During mission 2, with the estimated payload of 8.65lbs, at a cruise speed of 99 ft/s, the plane is expected to conduct between 8 and 9 laps in the five-minute flight window. Regarding Mission 3, it is important to note a decrease in the glide ratio also known as L/D, due to the extra drag stemming from the banner and its components.

. Table 20: Aircraft Performances for M1, M2, and M3

Parameter	Mission 1	Mission 2	Mission 3
Cruise Wing loading (lb/ft^2)	2.510	3.573	2.512
Cruise AoA (deg)	1.000	2.250	2.000
Cruise CL	0.224	0.306	0.289
Cruise CD	0.020	0.024	0.027
stall Speed (ft/s)	37.000	44.000	37.000
Cruise speed (ft/s)	95	95	66
Glide Ratio	11.2	12.750	10.547
Take off distance (ft)	75.000	179.000	75.000
Endurance (min)	9	6.5	7.000
Lap time (s)	30	37	32

5.6 Drawing Package

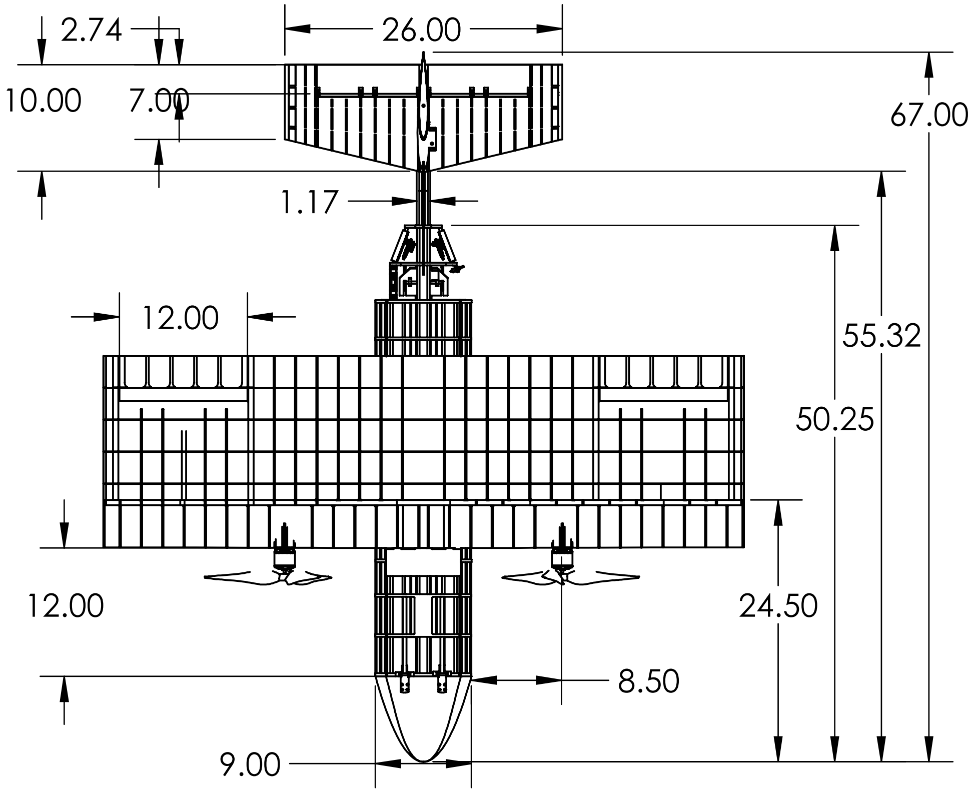

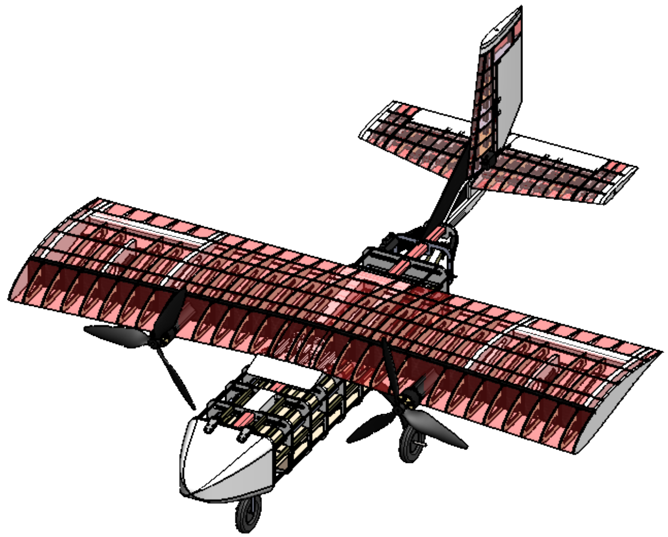

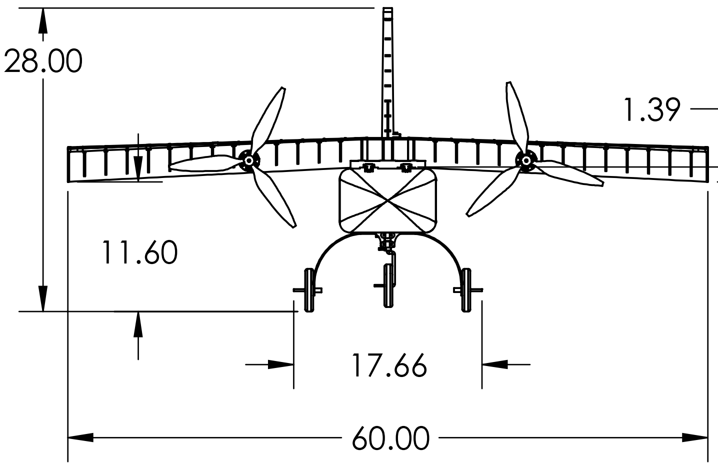

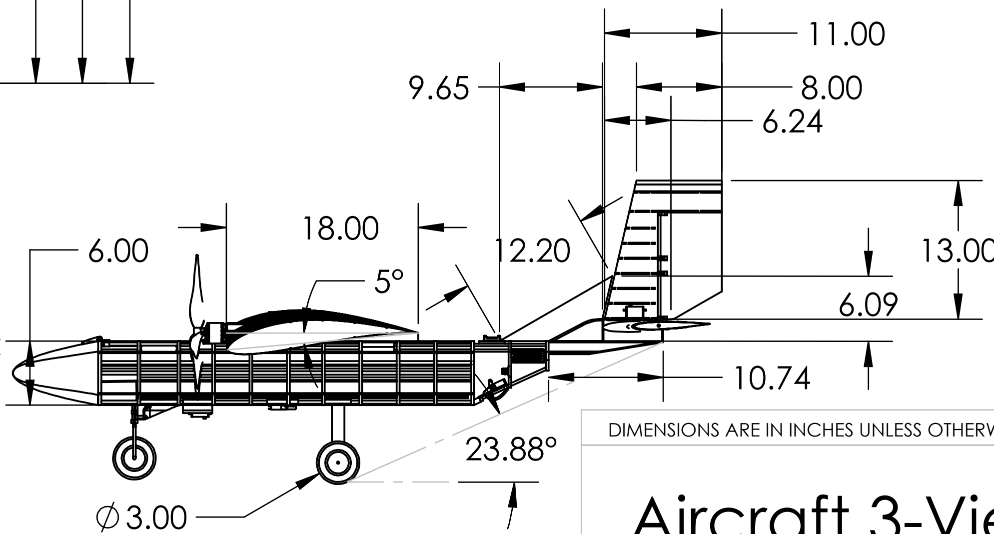

All dimensions are in inches.

DIMENSIONS ARE IN INCHES UNLESS OTHERWISE NOTED

Aircraft 3-View

SIZE
A

OU2026-1

SCALE: 1:18

SHEET 1 OF 4

ITEM NO.	PART NUMBER	DESCRIPTION	QTY.
1	Fuselage Frame	PETG	11
2	Nose Cone	PETG	1
3	Wing Rib	Balsa, PETG	30
4	Wing Mount	PETG	1
5	Main Wing Spar	Carbon Fiber, Nomex	1
6	Aileron	PETG	2
7	Fuselage Taper Frame 1	PETG	1
8	Fuselage Taper Frame 2	PETG	1
9	Horizontal Stabilizer	Balsa, PETG, ASA Aero, Carbon Fiber	1
10	Vertical Stabilizer	Balsa, PETG, ASA Aero, Carbon Fiber	1
11	Tail Mount	PETG	1
12	Fuselage Hockey Stick Spar	Carbon Fiber	1
13	Passenger Loading System	Carbon Fiber, Cardboard,PETG	1
14	Cargo Loading System	Cardboard	1
15	Wing Motor Mount	PETG	
16	Rear Landing Gear	Carbon Fiber, Rubber, Aluminum	1
17	Front Landing Gear	Rubber, PETG, Aluminum	1
18	Wing Stringers	Balsa	24
19	Banner Deployment	PETG	1
20	Strake	Carbon Fiber, Balsa	1
21	Towline Release	PETG	1

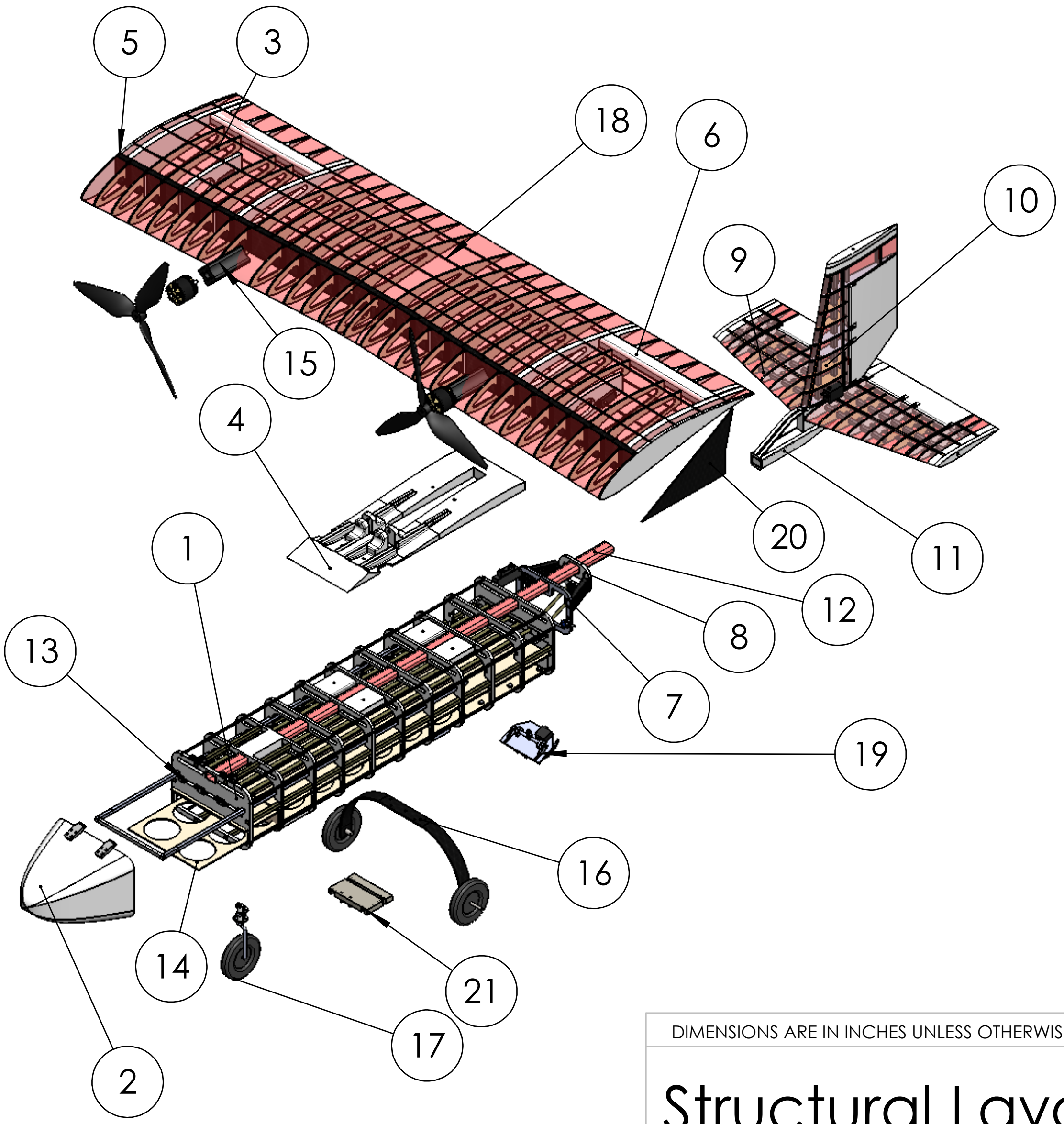

DIMENSIONS ARE IN INCHES UNLESS OTHERWISE NOTED

Structural Layout

SIZE A

OU2026-2

SCALE: 1:15

SHEET 2 OF 4

ITEM NO.	PART NAME	QTY.
1	Hockey Stick	1
2	Front Frame	1
3	Standard Frame	7
4	Front Landing Gear Frame	1
5	Taper Frame 1	1
6	Taper Frame 2	1
7	Balsa Wood Stringer	9
8	Carbon Fiber Square Spars	6
9	Passenger Removal	1
10	Cargo Tray	1
11	Passenger Tray	1
12	Carbon Fiber Circular Spars	6
13	Springs	6
14	Passenger Door	1
15	Cargo Door	1
16	Nose Cone	1
17	Nose Cone Hinge	2
18	Internal Wing Mount	2

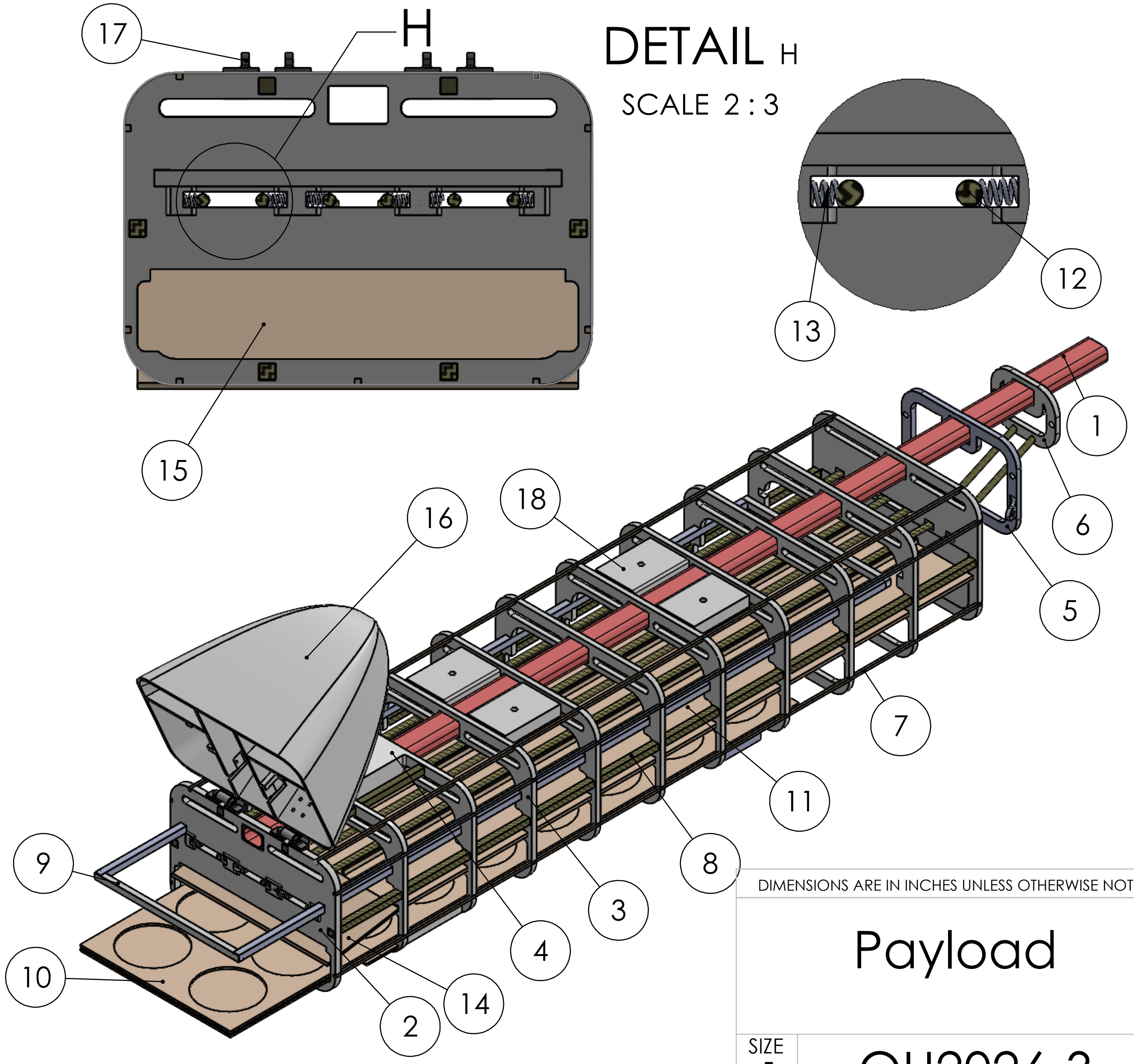

DETAIL H

SCALE 2 : 3

SCALE 1 : 6

DIMENSIONS ARE IN INCHES UNLESS OTHERWISE NOTED

Payload

SIZE **A**

OU2026-3

SCALE: AS SPECIFIED

SHEET 3 OF 4

ITEM NO.	PART NAME
1	Propulsion Battery
2	Receiver
3	Avionics Battery
4	Port Propeller
5	Starboard Propeller
6	Port Motor
7	Starboard Motor
8	Port Aileron Servo
9	Starboard Aileron Servo
10	Arming Fuse
11	Avionics Switch
12	Port ESC
13	Starboard ESC
14	Rudder Servo
15	Steering Servo
16	Towline Release Servo
17	Banner Deployment Servo
18	Elevator Servo

Systems Layout (1:20)

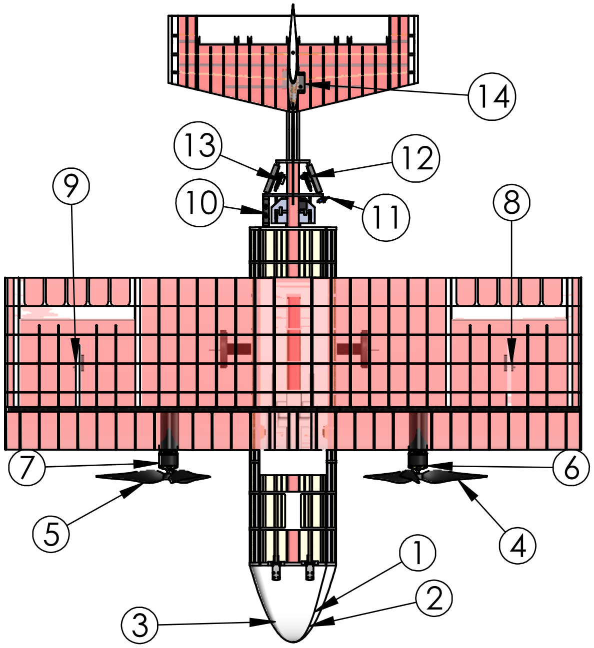

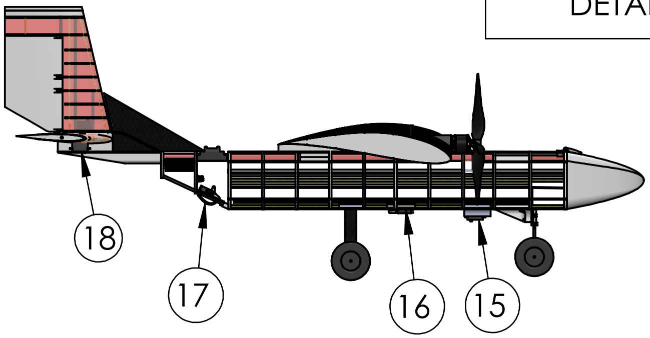

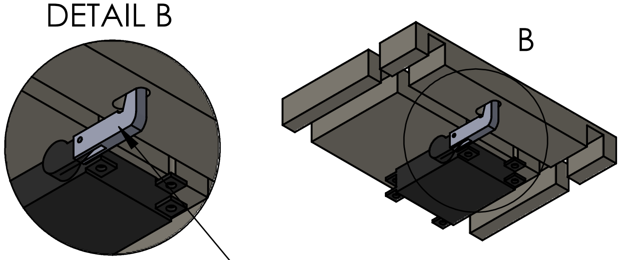

Towline Release Mechanism (1:3)

Towline Hook in closed (towlineattached) position

Banner Deployment Mechanism (1:3)

Banner Hook in closed (stowed) configuration

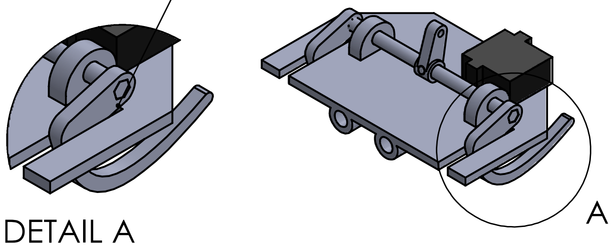

DIMENSIONS ARE IN INCHES UNLESS OTHERWISE NOTED

Electronics and Systems

SIZE
A
OU2026-4

Scale as Specified
SHEET 4 of 4

6.0 Manufacturing Plan

Through extensive research into materials and manufacturing processes, the team compiled several key contenders for manufacturing the aircraft, prioritizing strength, stiffness, and low weight, to effectively realize the detailed design.

6.1 Investigated Processes

6.1.1 3D Printing

3D printing includes gradual deposition of a plastic material to rapidly construct complex geometry, while being highly customizable to desired mechanical characteristics through careful plastic selection and print settings. It was considered due to its ease of fabrication, potential for rapid iteration, and being lightweight, yet stiff. Several plastic materials were considered, primarily due to their weight, toughness, and heat resistance. The key weakness identified with 3D printed components was their generally brittle nature and tendency to fracture in the chosen z-direction. PETG was identified as an ideal candidate for structural components, while ASA Aero was identified as a beneficial material for lightweight components.

6.1.2 Wooden Construction

Wooden construction from balsa wood primarily involves laser cutting and hand shaping to create precise geometries. It was considered for ease of fabrication, rapid iteration, low weight, and low cost. Through laser cutting, components can be manufactured rapidly with high precision, and through hand shaping, they can be further customized to adapt to errors in the manufacturing process. The primary weaknesses identified with balsa was poor load resistance and inconsistent densities across materials. Combined with other structural components, wooden construction was identified as being a strong candidate for internal, non-load bearing components.

6.1.3 Composite Manufacturing

Composite manufacturing involves flooding a fabric matrix with a thermoset plastic to augment the mechanical properties of both materials. It was considered due to its high strength-to-weight ratio, high stiffness, and highly customizable nature based on the material and weaving of the selected fabric. Carbon fiber, fiberglass, and aramid were considered as fabrics, while epoxy was the chosen binder. The main drawbacks of composites were the high cost and difficulty of manufacture. Carbon fiber was identified as the primary contender, due to its low weight and optimal stiffness.

6.1.4 Foam Construction

Foam construction involves shaping extruded polystyrene foam with a hot wire or sandpaper to subtractively create geometries. It was considered as a construction process due to its low density, low cost, and ease of manufacture. It was identified to be a strong choice for reinforcing structural components due to its favorable performance resisting distributed loads. The main drawback of foam was its poor stiffness and poor performance under direct loading.

6.1.5 CNC Milling

Computer Numerical Control (CNC) milling is a subtractive manufacturing process where materials, often metals, are shaved away to create detailed geometries. It was considered a construction process due to its high precision and the strength offered by metal components. The key weaknesses are the complexity of the manufacturing process, the high cost, and the high weight of the frequently used materials.

6.1.6 Process Down-Selection

The primary factors considered while selecting manufacturing processes and materials were ease of fabrication, speed of iteration, mechanical properties, and cost. Each criterion was rated 1-5, with 1 being suboptimal and 5 being ideal. Speed of iteration and mechanical properties were the primary focus, with ease of fabrication and cost being tiebreakers between process and material options. The trade study table shown in Table 20 details the scores of each process and corresponding materials. The table shows that the manufacturing of the aircraft should be centered primarily around 3D printing, wooden construction, and foam construction where able. Foam construction was eventually abandoned due to the volume of material that would be necessary in critical areas for wiring and storage. While composite manufacturing scored low, it was considered for key structural components, where the mechanical properties were assessed to be worth the financial and time cost associated with the process.

Table 21: Decision Matrix Justifying Manufacturing Processes Utilized

Process	Ease of Fabrication	Speed of Iteration	Mechanical Properties	Cost	Total Score
3D Printing	4	5	3	4	**14**
Wooden Construction	4	4	2	5	**15**
Composite Manufacturing	2	2	5	2	11
Foam Construction	4	3	3	5	**15**
CNC Milling	1	1	4	2	8

6.2 Manufacturing Processes

6.2.1 Wing

The wing was manufactured out of a carbon fiber sandwich spar, which was constructed on a flat 3D printed mold out of epoxy resin and carbon fiber fabric. The selected fabric was 4 plies of 3k plain weave fiber, which provided an optimal strength-to-weight ratio. The composite was made using wet layup processes and cured under a vacuum to allow the resin to fully saturate the fiber and reduce the chances of delamination. Two of these sheets and a sheet of Nomex honeycomb were glued together using DB420 epoxy adhesive to create a composite sandwich that offers ample stiffness and resistance to wingtip bending under typical flight conditions. Initially, the wing skin itself had also been made from carbon fiber composites, but this was removed in the second and final iterations due to weight and manufacturability concerns. For the ribs and internal supports, balsa wood was laser cut into stringers for the airfoil shape aft of the quarter-chord on either side of the spar, placed carefully to ensure that the airfoil is uninterrupted when the composite spar cuts off.

For more structural components, such as framing the ailerons, mounting the wing, and the endcaps of the wing, 3D printed PETG was used to provide more stability than balsa. PETG was selected for its high melting point, which ensures that there is no warping when heat is applied in other parts of the manufacturing process. Once the airfoils were glued into place, Ultrakote, a heat-shrink thermoplastic, was fixed to the surface. A heat gun was used to shrink the plastic into the airfoil shape, creating the smooth surface of the wing.

The ailerons were manufactured by 3D printing with PETG and then applying Ultrakote. They were attached to the wing via carbon fiber spars that were fixed in the ailerons and freely rotated within fixtures in the wing. The fixtures were mounted to the spar and the ribs to ensure control surface rigidity.

6.2.2 Fuselage

The fuselage was primarily comprised of a 3D-printed PETG skeleton. 3D printing was selected due to its ability to handle the geometries of the frame consistently and effectively. PETG was selected because it was already readily available to the team and is strong enough to support the weight of the fully loaded aircraft. The skeleton mounted to a carbon fiber hockey stick that acted as a structural backbone for the entire plane. The PETG ribs were tightly toleranced to fit the hockey stick and were placed equidistant down the length of the fuselage. Square carbon fiber spars were inserted into the ribs, providing additional stability down the length of the fuselage. On the exterior of the skeleton, divots were made in the PETG to house balsa wood stringers, that provided a structure for the outer skin of the fuselage to adhere to. The stringers were superglued into the divots. From there, a hot iron and heat gun were used to affix Ultrakote thermoplastic as a skin. By applying heat, the plastic was shrunk down to ensure a snug, uninterrupted fit.

6.2.3 Empennage

The empennage was built out of a combination of PETG and ASA Aero 3D printed components, balsa wood, carbon fiber spars, printer paper, and Ultrakote thermoplastic. 3D printed plastic and laser cut balsa were selected for their abilities to accurately create detailed and consistent geometries that are necessary in airfoils. The tail attaches to the fuselage's hockey stick backbone with a 3D printed adapter that is made from PETG. It was printed so that the strongest direction would be towards the nose of the plane to ensure that there is no delamination. Thin carbon fiber tubes were glued and bolted into this adapter to serve as spars running the length of the vertical and horizontal stabilizers. Small airfoils were then printed from PETG and ASA Aero plastics, to provide strength in key areas and general structural support in others. Along with identical pieces laser cut from balsa wood, the airfoils were inserted over the carbon tubes and fixed into place with super glue. Paper was glued to the leading edge of the stabilizers, to provide a smooth and clean surface for the Ultrakote outer skin to adhere to. A hot iron and heat gun were used to shape the Ultrakote thermoplastic into the skin of the tail, providing a smooth, low-drag surface.

The control surfaces were made from ASA Aero to keep the tail lightweight. They were fixed to the vertical and horizontal stabilizers via more carbon fiber tubes, which were fixed to the control surface but could rotate freely in their housings within the stabilizers. The control surfaces were fitted with servo horns to be able to effectively hinge when called.

The strake was made from balsa wood sandwiched between sheets of carbon fiber composite material. A wet layup was made on a 3D printed plate, with balsa applied to the fiber in the middle of the layup. The whole balsa and fiber combination was cured under a vacuum to ensure thorough lamination. The strake was then cut to size and bolted onto the empennage.

6.3 Manufacturing Schedule

A manufacturing milestone chart was created to ensure adherence to the overall project schedule. Lessons learned from the manufacturing schedules of previous prototype builds were incorporated to refine and optimize the timeline for the competition aircraft. The target completion date for each full prototype was established at the beginning of October, as shown in Fig. 40, which compares planned and actual timelines for each prototype build.

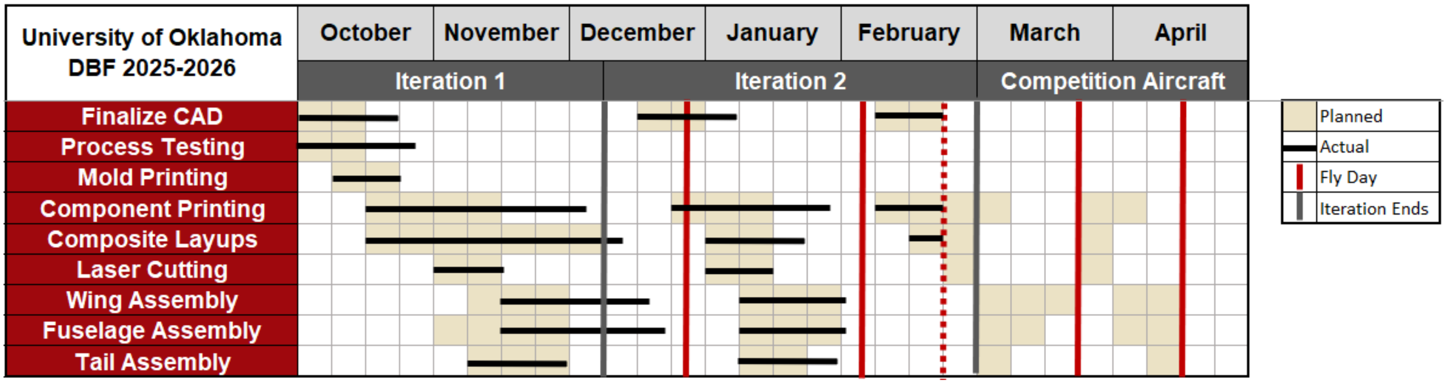

Figure 40: Manufacturing Milestone Chart

As shown in the Figure, the grey vertical lines indicate the originally planned iteration completion milestones, which serve as formal design freeze points between prototype phases. These milestones were defined when manufacturing and testing for each iteration were intended to conclude before transitioning into the next build cycle. While iteration 1 concluded near its projected end date, Iteration 2 reached flight readiness ahead of schedule. The earlier-than-planned flight test enabled the team to compress the development timeline and transition into an additional refinement phase that was not originally scheduled. This effectively created an Iteration 3 period, allowing for further weight reduction, structural improvements, and flight performance tuning before finalizing the competition aircraft configuration. The schedule flexibility gained through early completion reduced overall program risk and increased confidence in the final aircraft design.

7.0 Testing Plan

7.1 Objectives and Schedule

The schedule for testing the sub-system components and aerodynamic performance of the aircraft is outlined in Fig. 41.

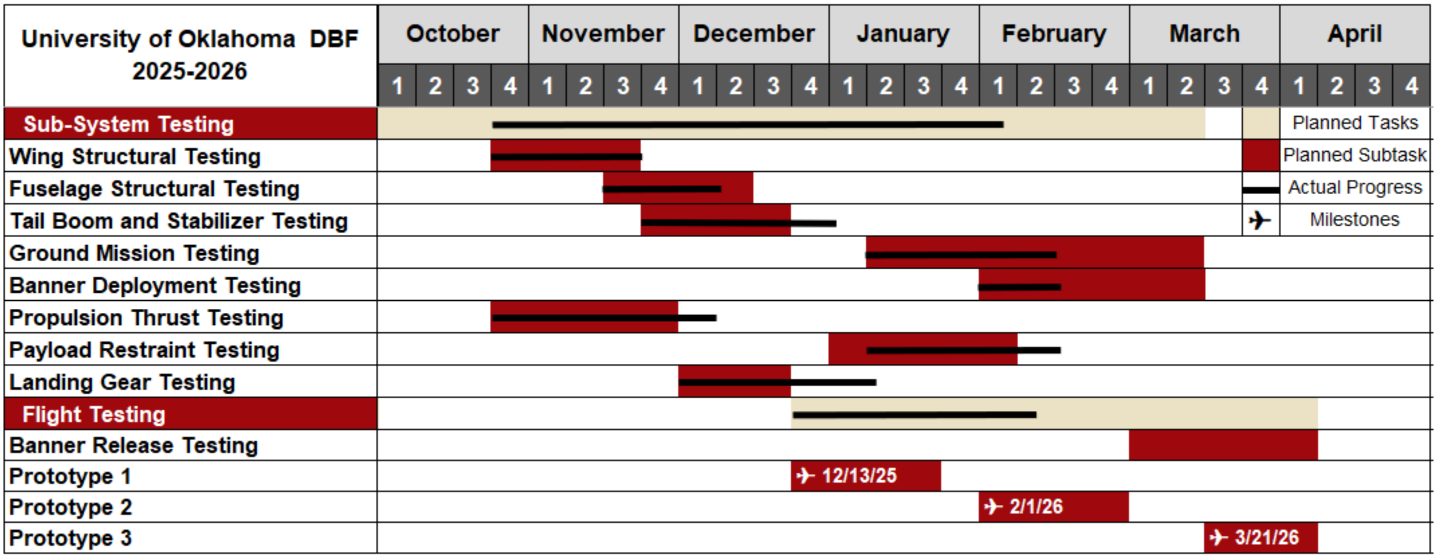

Figure 41: Testing Schedule

To ensure compliance with the defined design objectives, comprehensive ground and flight testing were performed on the aircraft and its subsystems. The objectives for each test are outlined below in Table 21. The results of the testing can be found in Section 8.

Table 22: Testing Objectives

Testing Category	Objectives
Aerodynamics	
FLIGHT TEST	Confirm predictions for lift, drag, and stability characteristics from XFLR5
	Get pilot feedback on the performance characteristics and maneuverability
Structures	
STRESS TESTING	Determine if the spars, wing, and tail have sufficient stiffness and strength to sustain the load
THRUST TEST	Determine that the motor mounts have sufficient strength to endure torque, shear force, and thrust at full throttle
FLIGHT TEST	Confirm that the fuselage can withstand the energy transferred from the landing gears
Banner Deployment and Payload	
DEPLOYMENT TEST	Test that the banner will deploy and fly in a vertical position while withstanding 1.2x the expected flight speeds
RELEASE TEST	Confirm if the banner drop and release mechanism performs reliably
GROUND MISSION TEST	Practice Ground Mission routines to minimize Ground Mission runtime.
Landing Gear	
TAXI TEST	Confirm that the front landing gear has sufficient stiffness and strength to withstand the maximum MTOW in taxi
LANDING TEST	Confirm that the rear landing gear can withstand the maximum MTOW landing loads
Propulsion	
BATTERY TESTING	Determine battery life, charging time, and discharge capabilities using a test stand and installed static testing
THRUST TEST	Compare theoretical thrust to real-world performance
Performance	
FLIGHT TEST	Observe time stamps, air speed data, ground roll data, and turning radius in real time using a Pitot tube, controller data, and other data recording devices

7.2 Sub-System Testing

7.2.1 Structural Testing

7.2.1.1 Wing Spar

To determine the ultimate load capacity of the wing spar, the wing was supported at the wingtips to allow the application of a load at the center of the span, incrementally increased by suspending weights directly from the spar. As shown in Fig. 42(a) The load was increased in 5–10 lb increments until structural failure occurred, allowing identification of the ultimate load and failure mode. To further evaluate structural robustness under concentrated loading, additional testing was conducted by having team members apply static body weight at mid-span and other critical locations along the wing, seen in Fig. 42(b). These tests provided qualitative validation of the spar’s ability to withstand localized loads representative of handling, transportation, and worst-case flight loading conditions.

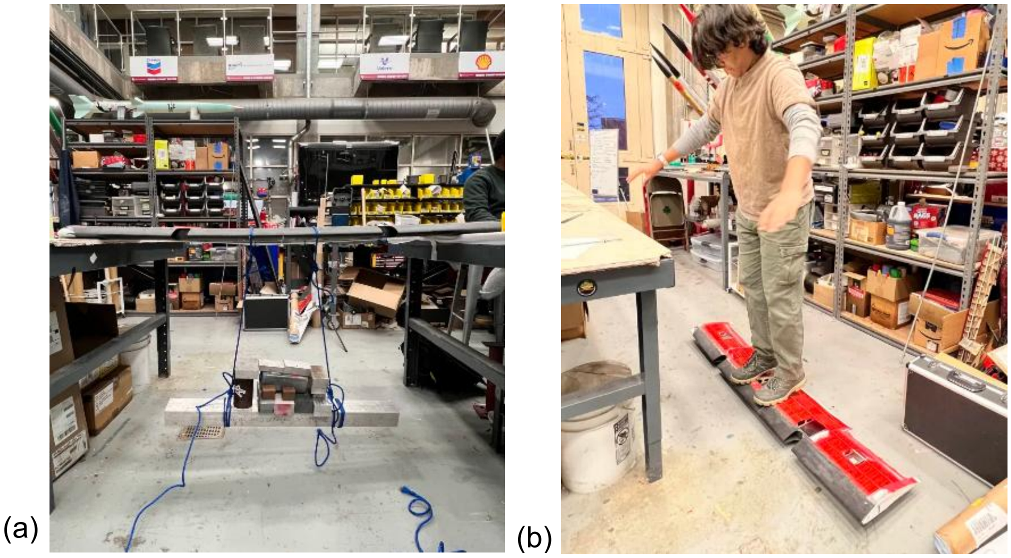
(a) (b)

Figure 42: Spar Loading Testing. Weight Added (Left) Members Weight (Right)

7.2.1.2 Fuselage Spar/Hockey Stick

The main load-bearing structure of the fuselage, a hockey stick, acts as the main spar and was tested by applying weight in increments of 10 lbs, up to 100lbs. It was also tested by standing on it with two points of contact as shown in Fig. 43 to the right.

43: Load Testing on Hockey Stick

7.2.2 Static Thrust Testing

Static thrust testing was performed for the selected propulsion system using a test stand. The apparatus features frame with a mounting surface for the motor which slides on a pair of low friction rods. A spring scale attached to the motor mounting surface allows measurements of static thrust. The testing was conducted by taking these measurements at throttle increments of 25% to compare them with eCalc suggested values. Fig. 44 shows a 3-blade 14x13 propeller with a 330 Kv motor, powered by a 6S 4400 mAh battery. The test was conducted at maximum throttle to estimate maximum thrust and minimum flight time.

7.2.3 Installed Thrust Testing

Installed thrust testing was conducted after the airframe construction was completed and the engine were mounted on the wing. The test was conducted by hooking a spring scale to the rearmost fuselage frame and then attaching it to a hard point. Like the static thrust test, the throttle was advanced at known increments to observe total aircraft thrust. In addition, this test was also intended to highlight any asymmetric thrust, or other flaws in engine mounting and installation.

Figure 44: Static Thrust Testing with Test Stand

7.2.4 Avionics and Range Testing

A radio-frequency range test was conducted to verify uninterrupted communication between the pilot and the aircraft during flight operations. The FrSky X8R receiver has a nominal operating range of 1640 yds. To evaluate effective system range, the RadioMaster TX16S transmitter was placed in range-test mode while the aircraft, equipped with the X8R receiver, was positioned on the airstrip. The transmitter was then moved progressively farther from the aircraft, while the received signal strength indicator was continuously monitored on the transmitter. This procedure confirmed reliable communication performance over the tested distances.

7.2.5 Ground Mission Testing

The Ground Mission timing test evaluated the efficiency and repeatability of the aircraft's cargo loading/unloading process and banner installation procedure. The purpose of this testing was to identify opportunities for improvement to maximize performance during the timed ground mission event.

Each stage of the ground mission was timed and repeated multiple times to establish representative average completion times. The evaluation included loading the passenger (rubber duck) and cargo (hockey puck) payloads into their designated bays, verifying proper placement and securement, and conducting controlled unloading procedures. Emphasis was placed on the accessibility of the fuselage bays, fastening efficiency, and coordination during the loading sequence.

Following payload operations, the banner system installation was performed, including attachment of the tow mechanism, routing and securing of the banner material, and verification of the deployment and release mechanism. The reliability and repeatability of the release system were assessed under time pressure to ensure consistent performance.

7.2.6 Banner Testing

The mission banner underwent an initial evaluation through ground-based testing designed to approximate aerodynamic loading. During this phase, the banner was extended from a moving vehicle to simulate airflow conditions. Observations from this setup indicated the need to reinforce the banner’s leading edge and incorporate a small weight at the bottom to maintain proper orientation.

Additional ground tests focused on validating the deployment and release mechanisms. The system demonstrated the ability to support the banner’s weight even when extra manual resistance was applied. The locking mechanism was also tested by applying tension to the string while the system remained secure, confirming that it could withstand turbulence and external forces without unintended release.

7.4 Pre-Flight Checklist

To support safe and consistent data collection, a checklist was developed to methodically confirm the condition of all aircraft components and define the flight test procedures for pre-flight, in-flight, and post-flight operations. Implementing the checklist shown in Table 23 helped reduce potential risks and increase overall flight reliability.

Table 23: Pre-Flight Checklist

Flight Briefing			
Pilot & FAA Number:		Date:	
Payload Configuration:		Flight Description:	
Total Aircraft Weight:		Flight Duration:	
CG from the nose (in.):		Wind Conditions:	
PREFLIGHT - NO POWER		**PREFLIGHT - POWER**	
Internal Systems		**Electrical Systems**	
Battery Voltages (V):		Receiver on	Y/N
Batteries, receiver, & ESC secured	Y/N	Failsafe control surface check	Y/N
Avionics & Sensors Installed	Y/N	Verify sensors are calibrated & logged accurately	Y/N
All internal wiring secured	Y/N	Telemetry and control range check	Y/N
Propellers secured	Y/N	Banner deployment avionics functional/control	Y/N
External Walkaround Inspection		Propeller Installed	Y/N
Wings, Ailerons, & Flaps secured	Y/N	Full Throttle Performance Test on Motor	Y/N
Vertical Stabilizer & Rudder Secured	Y/N	Download and Reset Controller Data Logs	Y/N
Horizontal Stabilizer & Elevator Secured	Y/N	**TAXI & BEFORE TAKEOFF**	
All Control Surface Linkages Secured	Y/N	Have a Brief of the Flight Plan	Y/N
Landing Gear Secured	Y/N	Wind Direction Verified & Aircraft Lined Up	Y/N
Passengers and Cargo Secured (M2 Only)	Y/N	Arm Aircraft & Final Control Deflection Check	Y/N
Banner & Release Mechanism Secured	Y/N	Verify Everyone is Ready & Clear for Takeoff	Y/N
Wing box and Fairing Secured	Y/N	**Post Flight**	
Fuselage Door Closed, Secured, Positive Hatch	Y/N	Aircraft Stopped & Disarmed	Y/N
Motors Secured	Y/N	Flight & Avionic Batteries Disconnected	Y/N
Verify no visual or feel-damages	Y/N	Pilot & Chief Engineer Written Debrief Complete	Y/N

Final flight authorization is determined through a Yes/No (Y/N) verification process performed during the preflight checklist. Each checklist item is evaluated and marked as satisfactory (Y) or unsatisfactory (N). Any unsatisfactory result in an automatic No-Go decision until the discrepancy is corrected and the item is verified. This approach ensures that critical functionality is fully validated prior to taxi and takeoff. Final launch authority is granted only when all critical systems are verified as satisfactory. These procedures are implemented in accordance with the flight and safety checklist expectations outlined in the AIAA DBF competition rules [1].

8.0 Performance Results

The following sections summarize the results of ground and flight testing described in Section 7.0. These tests were performed to verify the structural integrity, performance, capability, and durability of critical aircraft's ability to withstand expected aerodynamic, structural, and environmental loading throughout all phases

8.1 Demonstrated Performance of Key Subsystems

8.1.1 Aerodynamics

The aerodynamic flight test results exhibited strong correlation with the XFLR5 simulations, regarding stall characteristics and mission velocities. During initial flight evaluations of the first iteration, a performance discrepancy was identified where the aircraft experienced premature outboard flow separation, resulting in a loss of roll control and a subsequent design flaw analysis.

This behavior was mitigated in the second iteration through the integration of a 5° geometric washout and spanwise airfoil morphing. This configuration ensured that stall initiation was localized at the wing root, preserving attached flow over the ailerons and maintaining full roll authority at high angles of attack. Furthermore, while theoretical calculations predicted a stall velocity of 32 mph, flight validation demonstrated a reliable stall speed of approximately 25 mph.

This improvement in the low-speed flight envelope indicates that the high-lift root profile and aerodynamic fairing provided a more robust performance margin than the conservative XFLR5 simulations initially suggested. Consequently, the aircraft’s ability to maintain controllability at lower-than-predicted air speeds significantly enhances mission safety during the landing and recovery phases. Furthermore, the increased control authority from resized surfaces ensured that the aircraft remained responsive across all tested flight regimes, validating the transition from the initial design iteration to the current optimized configuration.

8.1.2 Propulsions

The static thrust test results showed strong agreement with eCalc predictions, as illustrated in Figure 38. At higher throttle settings, the measured thrust fell below the predicted values, which is attributed to propeller stalling under zero forward-velocity conditions. This behavior is expected for high-pitch propellers operating statically, where the blade sections experience excessive angles of attack. As forward airspeed increases during takeoff and climb, the effective angle of attack on the propeller blades decreases, alleviating stall and allowing thrust to recover toward predicted values. Consequently, static propeller stalls are not considered a significant performance limitation for the aircraft. Furthermore, the measured static thrust-to-weight ratio at gross takeoff weight was approximately 0.8, indicating sufficient thrust margin to ensure reliable takeoff performance.

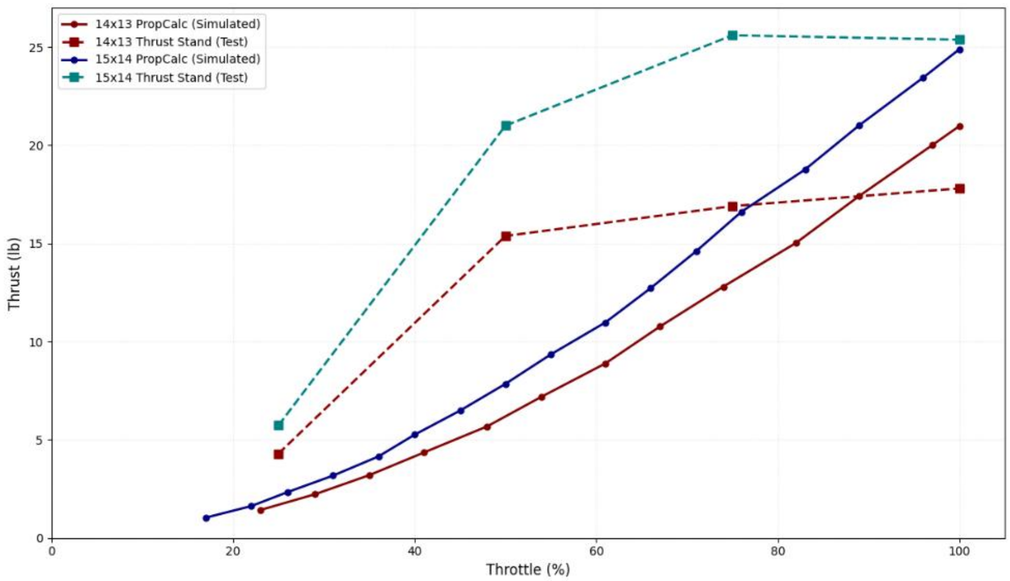

Figure 45: Static Thrust Test Results

Installed thrust testing was conducted after the motors were mounted on the wing, which initially revealed asymmetric thrust between the two propulsion systems. This asymmetry was attributed to two primary factors. First, aerodynamic vibrations occurred due to the propeller plane being positioned too close to the wing leading edge, resulting in unsteady inflow conditions. Second, one electronic speed controller intermittently entered a low-voltage cutoff state due to voltage sag in certain batteries under high current demand. These issues were mitigated by increasing the motor mount standoff distance to reduce aerodynamic interference and by individually testing propulsion batteries for current capability. Batteries exhibiting excessive voltage sag were removed from service and replaced, resulting in consistent and symmetric thrust performance.

8.1.3 Structures

8.1.3.1 Wing Spar

Testing showed initial signs of failure begin at 98 lbs. Overall, wing failure occurred at 170 lbs, but spar remained intact at that weight. Complete failure of the wing, including the spar, occurred at 200 lbs. This is well above our predicted load.

8.1.3.2 Fuselage Spar

Testing found the hockey stick was able to withstand over 155 lbs without breaking. This is well above our predicted load.

8.1.4 Avionics

Avionics and radio-frequency range testing confirmed reliable operation of all onboard electronic systems across the full range of expected flight distances. Stable communication between the transmitter and receiver was maintained without signal dropouts, and all control surfaces responded consistently and predictably throughout the test envelope. Following successful verification of system reliability, control surface sensitivities and transmitter mixing were incrementally adjusted based on pilot feedback. These refinements optimized control responsiveness, reduced pilot workload, and improved handling qualities across all mission configurations, resulting in smoother maneuvering and enhanced overall flight controllability.

8.1.5 Banner

Flight testing was conducted after the banner's structural modifications were completed. When attached near the aircraft's aerodynamic center, the banner introduced additional drag that caused the aircraft to fly at a reduced speed and required wider turning radii. Despite these changes, the aircraft maintained stable handling characteristics and performed reliably throughout the test flights.

These results indicate that the aircraft can operate effectively with the banner installed, though flight maneuvers must be adjusted to account for the increased aerodynamic resistance and altered turning performance.

8.2 Demonstrated Flight Performance of Completed Aircraft

Because of the absence of an Inertial Measurement System, part of the validation of the aircraft performance was done through the review of flight footage and imagery at several points. The observable characteristics were the trim angle of attacks.

Fig. 46 shows the completed aircraft in its ground configuration prior to takeoff. This configuration verifies the final center of gravity placement and payload integration for the demonstrated mission configuration.

Figure 46: Completed Aircraft in Ground Configuration Prior to Takeoff

Following takeoff, steady trimmed flight conditions were recorded and analyzed frame-by-frame to approximate trim angle of attack. Figs. 47(a) and 47 (b) show representative steady-level flight for the competition configuration. The observable fuselage pitch attitude relative to the horizon was used as a proxy for trim angle of attack (AoA).

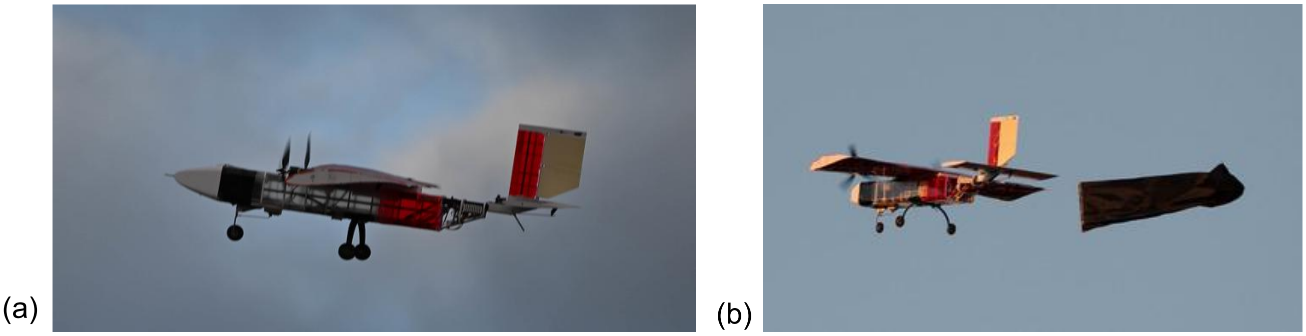

Figure 47: Representative Steady Trimmed Flight used for AoA Estimation. M1 (Left) and M3 (Right)

The performance closely matched the XFLR5 models with the corresponding center of gravity placements. The table below summarizes the angle of attacks observed versus the predicted values for configurations of each of the missions.

Table 24: Predicted vs Actual angle of attacks

Parameter	Mission 1	Mission 2	Mission 3
Predicted trim AoA (°)	2	0.75	4
Observed trim AoA (°)	2~5	1~2	5~7

Bibliography

[1] American Institute of Aeronautics and Astronautics, *2026 Design/Build/Fly Rules*, AIAA, Reston, VA, Aug. 2025. URL: https://www.aiaa.org/wp-content/uploads/2025/08/2026-DBF-Rules.pdf

[2] Lennon, A., *Basics of R/C Model Aircraft Design: Practical Techniques for Building Better Models*, Air Age Media, Ridgefield, CT, 1996.

[3] Sadraey, M. H., Aircraft Design: A Systems Engineering Approach, Chichester, West Sussex: Wiley, 2013.

[4] XFLR5 Development Team, “XFLR5,” https://www.xflr5.tech/, accessed 19 Feb. 2026.

[5] D. Scholz, *Empennage Sizing Methods*, Hamburg University of Applied Sciences (HAW Hamburg), Department of Automotive and Aeronautical Engineering, Hamburg, Germany, 2013.

[6] ANSYS, Inc., “ANSYS Workbench,” https://www.ansys.com/products/ansys-workbench, accessed 19 Feb. 2026.

[7] Mueller, T. J., and DeLaurier, J. D., “Aerodynamics of Small Vehicles,” *Annual Review of Fluid Mechanics*, Vol. 35, 2003, pp. 89–111.

[8] Furlong, G. C., and McHugh, J. G., “Flight Investigation of Wing Fences as a Means of Improving Lateral Control Near Stall,” NACA Report 1022, 1950.

[9] Liebeck, R. H., “Design of Subsonic Airfoils for High Lift,” NASA Technical Memorandum TM-78411, 1978.

[10] Smith, A. M. O., “High-Lift Aerodynamics,” *Journal of Aircraft*, Vol. 12, No. 6, 1975, pp. 501–530.

[11] Zhang, Y., Wang, Z., and Li, Q., “Numerical Investigation of Winglet and Endplate Effects on Induced Drag Reduction,” *Aerospace Science and Technology*, Vol. 58, 2016, pp. 328–339.

[12] Müller, M., “eCalc – Electric Drive Calculator,” https://www.ecalc.ch/, accessed 19 Feb. 2026.

[13] U.S. Department of Defense, *Flying Qualities of Piloted Airplanes*, Military Specification MIL-F-8785C, Washington, DC, 1980.